Ocean Engineering 110 (2015) 339–356

Contents lists available at ScienceDirect

Ocean Engineering

journal homepage: www.elsevier.com/locate/oceaneng

Investigation on Darrieus type straight blade vertical axis wind turbine with flexible blade

Wendi Liu, Qing Xiao *

Department of Naval Architecture, Ocean and Marine Engineering University of Strathclyde, Glasgow, G4 0LZ, UK

ARTICLE INFO

Article history:
Received 27 June 2015
Accepted 17 October 2015
Available online 10 November 2015

Keywords:
Vertical axis turbine
Fluid structure interaction
Flexible material

ABSTRACT

In this study, a three-dimensional VAWT with a spanwise passively deformable flexible blade has been modelled. The study mainly focuses on the analysis of blade structure characteristics associated with the bending and twist deflection. Two types of flexible blade material and two strut locations supporting H-type blades are being investigated. The unsteady external loads and energy efficiency of VAWT with such designed flexible blade are also being analysed. The simulation results show that the bending and twist deflection peak is positively correlated with the turbine tip speed ratio λ. For a flexible blade, an unevenly distributed structural stress along the blade with a high stress regime in the vicinity of strut location has also been observed. Due to the rotational motion of a VAWT, the centrifugal force acting on VAWT blade plays an important role on the blade structure characteristics. Reduction of the blade stiffness results in an increase of the blade stress. Changing the strut location from middle to tip will cause a large area under high stress. The results also indicate that the VAWT with a highly flexible blade is not an efficient energy extraction device when it is compared to a less flexible or a rigid blade.

1. Introduction

With the increasing of the severe pollution generated by traditional fossil fuel, nowadays, people have been researching tremendously into renewable energy due to its clean and sustainable properties. Wind energy is one of the most popular types of renewable energy sources. There are two major types of wind energy converters, i.e. Vertical Axis Wind Turbine (VAWT) and Horizontal Axis Wind Turbine (HAWT). Compared with the HAWT, VAWT has many advantages, such as simple blade design and able to work in all fluid flow directions (Scheurich and Brown, 2013; Wenlong et al., 2013; Micallef et al., 2014).

In recent years, to achieve a large power output requirement and reduce environmental impact, there is an increasing trend to develop large scale tidal/wind turbines and move them far away to offshore areas (Hansen, 2013; Lachenal et al., 2013). Compared to the small scale and near shore devices, these large scale turbine blades/rotors may experience highly unsteady load due to turbulent wind flow in the offshore area especially under extreme weather conditions. This may lead to the possible deformation of blades, and thus reduces the turbines structural endurance.

To overcome this weakness, new types of composite material have been developed recently. The typical feature of these materials is the ability to deform adaptively to the unsteady loading exerted on it so that a more constant and uniform structure stresses on the turbine blades and shaft could be achieved. This could significantly increase the turbines fatigue endurance, and thus its reliability and sustainability for a long life cycle (Kong et al., 2005; Shokrieh and Rafiee, 2006; Barlas et al., 2008).

Kong et al. (2005) proposed a medium scale blade made of composite material using E-glass/epoxy for a 750 kW horizontal axis wind turbine, aimed to endure large loads onto the blade. Structural analysis with a Finite Element Method (FEM) model confirmed that the proposed blade with the new structure was able to tolerate variable load conditions as well as extreme flow conditions. The full scale static structure experimental test also obtained agreeable conclusions as the analytical results. The study by Shokrieh and Rafiee (2006) on the estimation of the fatigue life cycle of a horizontal axis turbine with composite material blades showed an averaged 22 years life of a HAWT using composite material blades while the traditional horizontal axis turbine with rigid blade is only 20 years life (Chenna, 2014). A wind tunnel test was performed by Barlas et al. (2008) for an adaptive HAWT blade, of which the trailing edge was designed as a piezoelectric bender. Their results indicated a significant reduction of blade stress and strain near its root with such design.

It is worthy to mention that, the flexible material is already being used to build up a HAWT blade as a so-called “Morphing Blade” (MB). MB has a specific feature to change its shape according to external aerodynamics loadings. It is used as a passive pitch control

* Corresponding author. Tel.: +44 141 5484779.
E-mail address: qing.xiao@strath.ac.uk (Q. Xiao).

http://dx.doi.org/10.1016/j.oceaneng.2015.10.027
0029-8018/

Nomenclature

$\overline{c}$	turbine chord-radius ratio which defined as $\overline{c}=\frac{c}{R}$
c	blade chord length (m)
c_c	centrifugal forces coefficient
c_{eff}	effective chord length for flexible material (m)
c_f	total fluid force coefficient which defined as $c_f=\frac{F_f}{\frac{1}{2}\rho_f U^2 cH}$
c_{ft}	total force coefficient which defined as $c_{ft}=\frac{F_{ft}}{\frac{1}{2}\rho_f U^2 cH}$
c_l	lift coefficient which defined as $c_l=\frac{liftforce}{\frac{1}{2}\rho_f U^2 cH}$
c_d	drag coefficient which defined as $c_d=\frac{dragforce}{\frac{1}{2}\rho_f U^2 cH}$
c_m	moment coefficient which defined as $c_m=\frac{M}{\frac{1}{2}\rho_f U^2 R^2 H}$
c_n	normal force coefficient
c_{op}	time averaged power coefficient
c_{pr}	pressure coefficient
c_{st}	stress coefficient
c_t	thrust coefficient
D_{is}	blade displacement at each point (m)
E	Young's modulus (Pa)
F_f	total fluid force (N)
F_{ft}	total force (N)
F_n	normal force (N)
F_t	thrust force (N)
F_c	centrifugal force (N)
f_r	turbine blade natural frequency at each mode (Hz)
$f_{5.5}$	turbine rotational frequency with tip speed ratio of 5.5 (Hz)
H	blade span length (m)
l_{st}	length from blade strut to its nearest blade tip (m)
M	blade moment relative to the turbine center (Nm)
p	local pressure (Pa)
p_∞	incoming fluid pressure (Pa)
R	turbine radius (m)
Re	turbine Reynolds number based on blade chord length
t	instant time (s)
T_{turb}	turbine revolution period (s)
T_{m1}	blade 1st bending mode period of region a and c (s)
T_{m2}	blade 1st bending mode period of region b (s)
T_{m3}	blade 1st torsion mode period of region a and c (s)
T_{m4}	blade 1st torsion mode period of region b (s)
T_{m5}	blade 1st bending mode period of tip strut condition (s)
T_{m6}	blade 1st torsion mode period of tip strut condition (s)
T_{m7}	blade 2nd bending mode period of region a and c (s)
T_{sf}	thickness of metal stiffener (m)
U	incoming flow velocity (m/s)
$V_t(t)$	blade instantaneous resultant velocity (m/s)
$x_l o_l y_l$	body fitted coordinate
$\alpha(t)$	blade instantaneous angle of attack (deg)
λ	tip speed ratio
ν	Poisson's ratio
σ	structure principal stress (Pa)
Π	effective stiffness
Π_r	blade natural frequency ratio in each mode defined as $\Pi_r=\frac{f_r}{f_{5.5}}$
ρ_f	fluid density (kg/m^3)
ω	turbine angular velocity (rad/s)

mechanism to ensure a satisfactory angle of attack for HAWT at the off-design wind speed conditions.

Despite the advantage of such new material and research on its application for HAWT, the investigation of the potential application of composite material onto VAWT is limited. This is partially because of the even larger variation of unsteady loads applying on a VAWT blade during its cyclic rotational motion as compared to a HAWT. Recently, Hameed and Afaq (2013) designed and studied a straight VAWT blade by using both analytical and numerical solutions. The bending deformation in the spanwise of the blade was allowed, and the structural stress distribution was investigated for the blades with different thicknesses under maximum fluid load conditions. In their study, a uniformly distributed external load along the span direction was assumed with its location at one quarter of leading edge. The centrifugal force was taken into account. Depending on the bending deflection and structure stress, an optimal thickness of the blade was predicted to achieve a minimum stress. More recently, Butbul et al. (2015) carried out a series of experimental tests and FEM analysis on a VAWT with a chordwise flexible blade. The study covered a prediction of blade morph direction, magnitude and their effects on the power generation. Their results showed that a better performance was observed by using a chordwise flexible morph blade at low tip speed ratio, which is very helpful to improve the self-starting ability of a VAWT compared to a rigid design VAWT. However, at large tip speed ratio, the performance of VAWT using a flexible morph blade decreases. It has also been observed that the centrifugal force of the blades has a significant impact at large rotational speed which leads to an outward blending motion of blade, and thus an increased drag force which further reduces turbine energy extraction.

It is well known that most of nature's creatures which can fly or swim are equipped with their flexible or deformed wings and bodies. They utilize this flexible feature to achieve high propulsion efficiency and manoeuvring capability. Many investigations have been conducted to study the wing flexibility impact on its propulsion characteristics. For example Heathcote and Gursul (2007) and Heathcote et al. (2008) designed a realistic internal structure for passive flexible flapping wings to test its propulsion performance by using both experimental and numerical methods. An enhancement of the propulsion efficiency has been observed with the flexible motion. Liu et al. (2013) investigated the potential benefits of a flexible oscillating foil on its energy extraction performance compared with the rigid one. Peak increment and phase lag effects on the instantaneous lift force were observed by the flexibility of the oscillating foil which could enhance the energy absorb efficiency of it. Le and Ko (2015) investigated the energy extraction performance for an oscillating hydrofoil with both chordwise and spanwise flexibility. A prescribed flexibility motion was used in their study and an up to 30% improvement in the power extraction efficiency was observed. However, despite some recent studies on the flexible wing for propulsion and energy extraction, there is still lack of work on detailed investigation of blade flexibility for vertical axis turbines.

In the present study, a three-dimensional vertical axis wind turbine with a flexible blade passively deformed in its span-wise direction has been numerically investigated. Realistic model of internal structures is used to obtain a certain degree of flexibility for the turbine blade. The main objective of the present study is to investigate the aerodynamic and structural behaviour of a VAWT with a flexible

blade. The blade structural deflection associated with bending and twist is mainly investigated at two flexibilities and strut locations. External unsteady loads onto the blade surface and power performance of VAWT are firstly studied, which is further extended to a blade stress analysis.

In the rest of the paper, the problem formulations and numerical modelling methodologies are listed in Section 2. In Section 3, we firstly investigate the structural characteristics of the flexible turbine blade in Section 3.1, the external loads onto the flexible blade is studied in Section 3.2. In Section 3.3, we extend our study to a more flexible blade and the impact of two different strut locations on the flexible blade is examined in Section 3.4, which is followed by an analysis of energy extraction performance of a flexiblly designed VAWT in Section 3.5. Finally, the conclusions of the studies are summarised in Section 4.

2. Problem formulation and numerical methodology

2.1. Problem description

Present study considers a three-dimensional Darrieus type straight blade vertical axis turbine with a NACA0012 cross-section blade and a passive bending and twist deflection in the blade span-wise direction. The pitch angle of the turbine blade is fixed as zero. A realistic internal structure is adopted from Heathcote et al. (2008), Chimakurthi et al. (2009) and Gordnier et al. (2010) to achieve blade passive deformation. The chord radius ratio (c) is 0.125 for the modelled turbine. The turbine, with a certain rotational speed, is immersed in air flow with a uniform speed of U. The Reynolds number based on blade chord length is 10^5. The Darrieus type straight blade VAT modelled by Hameed and Afaq (2013), shown in Fig. 1(a) consists of one shaft,

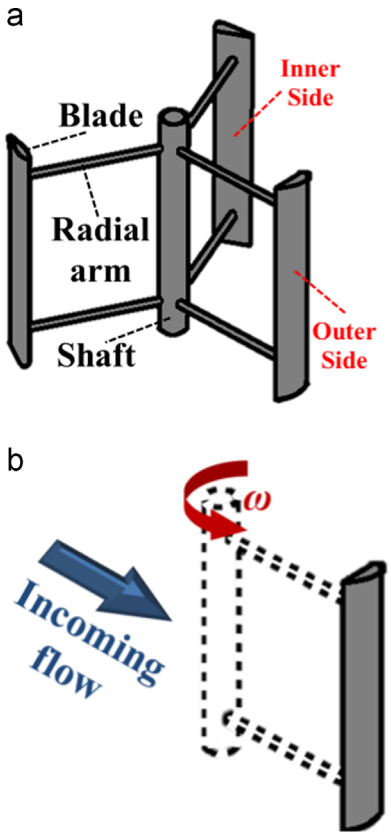

Fig. 1. 3D VAT model for (a) Hameed and Afaq (2013) and (b) in present simulation. (a) Darrieus type straight blade VAT model in Hameed and Afaq (2013). (b) VAT model in the present simulation.

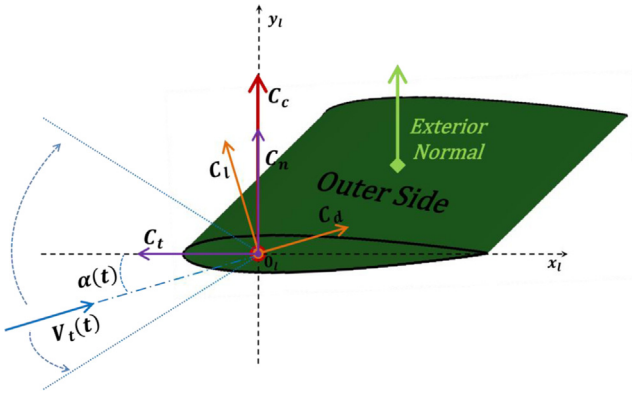

Fig. 2. Sketch of turbine blade forces, resultant velocity and angle of attack under local body fitted coordinate $x_l o_l y_l$.

three blades and six radial arms. The radial arms connect the shaft at one end and the Inner side of the turbine blade at another end. In order to simplify the physical model, only one blade is modelled in the present study. The aerodynamic impact from the shaft and radial arms are neglected as shown in Fig. 1(b). In this study, we mainly focus on the analysis of structural characteristics of flexible blade as well as the unsteady loads applied to the blades, which may cause the blade structural deformation.

2.1.1. Kinematics for vertical axis turbine

As shown in Fig. 1(b), the turbine is rotating with an angular velocity ω in the incoming flow. In the present study, we focus on the steady state of turbine and the startup and cutoff stage are ignored. Thus, the angular velocity ω is independent of time but varying under different tip speed ratios. In order to quantify the rotational speed of the turbine, the non-dimensionalized tip speed ratio λ is introduced and defined as follows:

$$\lambda = \frac{\omega R}{U} \tag{1}$$

where R is the turbine radius, U is the velocity of incoming air flow. In the present study, λ is changed in the range of 2.50–7.50 by varying the turbine rotational speed. Fig. 2 shows the blade local body fitted coordinate $x_l o_l y_l$ and the force applied on the blade, the resultant velocity and the angle of attack of blade. The origin of this local coordinate is fixed at the blade centre line and ¼ from the leading edge. The body fitted coordinate is attached to the turbine blade with rotating motion under global coordinate system. At $t/T_{turb}=0$, the direction of incoming flow velocity is the same as the positive y_l axis under body fitted coordinate. The magnitude of blade instantaneous resultant fluid velocity $V_t(t)$ and its direction (i.e. the blade instantaneous angle of attack $\alpha(t)$) are both varying with time as a sinusoidal function (Wang, 2005). The total fluid forces could be decomposed as the drag force and lift force or thrust force and normal force relative to instantaneous velocity or body fitted coordinate, respectively. Since the local coordinate is a non-inertia reference frame, it encounters an inertia force which is centrifugal force in the present case. The non-dimensionalized centrifugal force is defined as:

$$c_c = \frac{F_c}{\frac{1}{2}\rho_f U^2 cH} \tag{2}$$

where F_c is the centrifugal force of the turbine blade, ρ_f is the density of fluid, c is the chord length of the blade and H is the span length of the blade. The detailed comparison on the centrifugal force and fluid forces is listed in Table 1. An example of the comparison among the centrifugal force coefficient c_c, total fluid force c_f and the total force coefficient c_{ft}, which takes both fluid force and centrifugal force into account during one turbine rotating cycle could be found in Fig. 3.

Table 1
Past relevant research on flexible blade and the parameters used in the present research.

data source	device type	Π	max. c_f	c_c	max. D_{is}/c_{eff}
Heathcote et al. (2008) and Shyy et al. (2010)	Plunging foil (spanwise flexibility)	2.14E+02	4.76E+00	–	1.23E−01
Butbul et al. (2015)	Vertical axis turbine (chordwise flexibility)	3.18E+00	3.53E+00	7.10E+00	1.71E−01
Hameed and Afaq (2013)	Vertical axis turbine (spanwise flexibility)	2.81E+05	8.55E+01	4.31E+02	3.58E−02
The present research	Vertical axis turbine (spanwise flexibility)	3.19E+03	1.42E+02	1.24E+02	1.53E+00

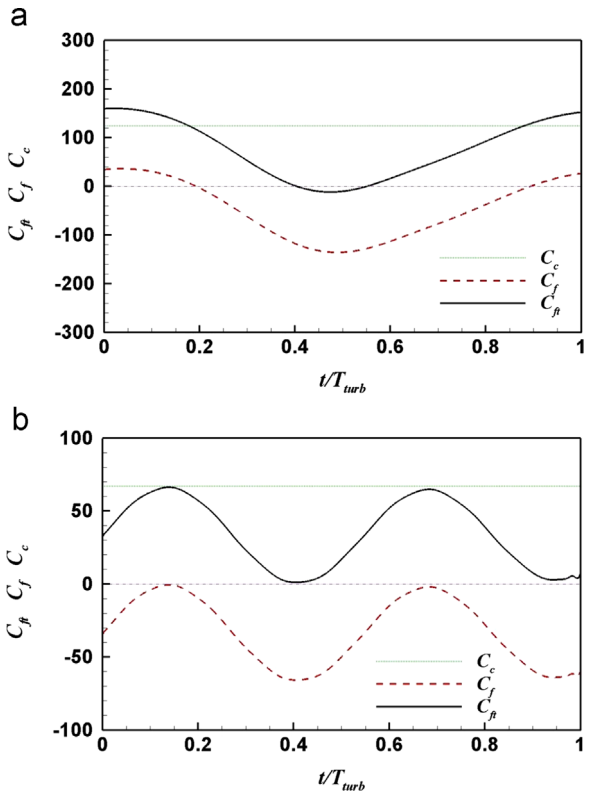

Fig. 3. An example of comparison between blade total force coefficient (c_{ft}), fluid force coefficient (c_f) and centrifugal force coefficient (c_c) with $l_{st}/c=\frac{10}{3}$, $\Pi = 3.19 \times 10^3$. (a) λ=7.5. (b) λ=5.5.

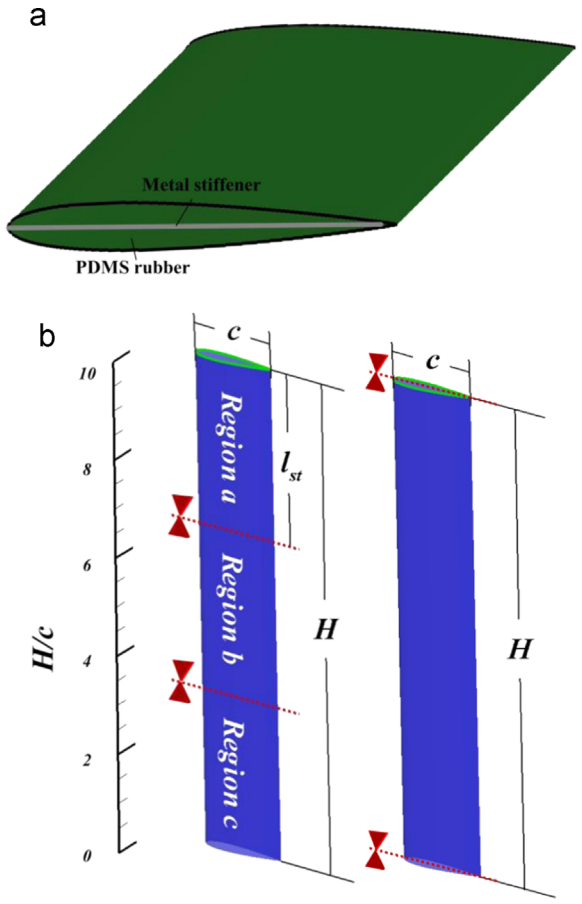

Fig. 4. VAT blade design for present simulation. (a) VAT blade inner structure (adopted from Heathcote et al. (2008)). (b) Different strut location for VAT blade. $l_{st}/c=\frac{10}{3}$ (left); $l_{st}/c=0$ (right).

2.1.2. Structural design of turbine blade

In the present study, we adopted the same concepts based on the study for a flexible effect on the propulsion performance of a flapping wing from Heathcote et al. (2008), Gordnier et al. (2010) and Chimakurthi et al. (2009), and further applied this flexible structure into our vertical axis wind turbine. The cross-section of blade is displayed in Fig. 4(a). The flexible blade is constructed by polydimethylsiloxane rubber (PDMS) outside to form NACA0012 shape with a metal stiffener locating inside. Aluminium is selected as the material of the metal stiffener. Based on Chimakurthi et al. (2009), only metal stiffener is considered in the structural dynamic analysis and the structural dynamic characteristics of the PDMS rubber is neglected in the present study (Liu et al., 2015).

Fig. 4(b) shows the main blade parameters with different strut locations. The span length H of the turbine blade is ten times of blade chord length c. The parameter l_{st} is defined as the length from the strut location to its nearest blade tip. In our present study, two different l_{st}, i.e. $10c/3$ and 0, are studied. For $l_{st}=10c/3$, three different regions, i.e. region a, region b and region c which are separated by two struts are shown in Fig. 4(b).

An important parameter, quantifying the stiffness of the structure, is effective stiffness Π (Shyy et al., 2010). This parameter describes the elastic bending forces relative to the fluid dynamic forces and is defined as:

$$\Pi = \frac{ET_{sf}^3}{12(1-\nu^2)\rho_f U^2 c^3} \tag{3}$$

where E is Young's modulus, T_{sf} is the thickness of metal stiffener and ν is the Poisson ratio of the stiffener.

In the study of Heathcote et al. (2008) and Shyy et al. (2010), Π is selected around 10^2 for their flexible wing under propulsion conditions. This value of Π allowed their wing to reach a maximum non-dimensionalized displacement D_{is}/c as 1.23×10^{-1}. However, it is necessary to recall that the blades of VAT have an extra inertia centrifugal force because of the rotating motion around the centre shaft. Moreover, the total fluid force coefficient acting on the VAT blade is around 10^2 which is much larger than that of propulsion flexible wing. Thus, adopting the same magnitude of Π as in the study of Heather et al. (2008) may lead to an unacceptable large blade displacement for a VAT. In the study of Butbul et al. (2015), a chordwise flexible blade is considered which is different as the design of a spanwise flexible blade as discussed in Shyy et al. (2010). In addition, the turbine they

studied was in small scale (as can be seen from Table 1 that both the maximum c_f and c_c are no more than 10^1). Thus, the Π selected by Butbul et al. (2015) may not be suitable for the present study. In the study of Hameed and Afaq (2013) for a bending motion of blade of VAT, a much stiffer blade is investigated with Π of 10^5, which caused a relatively small D_{is}/c of 3.58×10^{-2}. In the present study, in order to observe a distinct influence by the flexible VAT blade, the effective stiffness (Π) is chosen around 10^3, as shown in Table 1. The maximum non-dimensionalized displacement D_{is}/c under $\Pi = 3.19 \times 10^3$ and $\lambda = 5.5$ (i.e. the turbine reaches its maximum energy extraction) is 7.26×10^{-1} which is in the same order as that studied by Heathcote et al. (2008) and Shyy et al. (2010). The maximum D_{is}/c could approach 1.53×10^0 with $\Pi = 3.19 \times 10^3$ and $\lambda = 7.5$ as depicted in Table 1. A smaller effective stiffness $\Pi = 9.37 \times 10^2$ is also investigated in present research.

2.1.3. Fluid force coefficients

Several key parameters which quantify the turbine energy extraction performance are described below:

The normal force coefficient c_n and thrust coefficient c_t are defined by

$$c_n = \frac{F_n}{\frac{1}{2}\rho_f U^2 cH} \tag{4}$$

and

$$c_t = \frac{F_t}{\frac{1}{2}\rho_f U^2 cH} \tag{5}$$

where F_n and F_t are normal force and thrust force, respectively.

The time-mean power coefficient c_{op} is determined by

$$c_{op} = \frac{\overline{M\omega}}{\rho_f U^3 RH} \tag{6}$$

and the pressure coefficient c_{pr} is determined by

$$c_{pr} = \frac{p - p_\infty}{\frac{1}{2}\rho_f U^2} \tag{7}$$

where p and p_∞ are the local and far stream fluid pressure, respectively.

2.2. Mathematical formulations and numerical algorithm

Present simulation is performed by using our in-house FSI code. More detailed information about this in-house code could be found in our past papers such as Xiao et al. (2012) and Liu et al. (2013). There are some other references using similar numerical methodologies for the Fluid-Structure Interaction problems, such as Sadeghi et al. (2004), Im et al. (2012) and Bazilevs et al. (2015). A flow chart presented in Fig. 6(a) shows the modelling strategy with more detailed information to be listed in the following sections.

2.2.1. Fluid dynamics

Our fluid solver is based on the following governing equations of unsteady turbulence flow

$$\frac{\partial}{\partial t}\iint_\Omega \boldsymbol{W} d\Omega + \oint \boldsymbol{f} dS_x + \boldsymbol{g} dS_y + \boldsymbol{h} dS_z = \oint \boldsymbol{f}_\mu dS_x + \boldsymbol{g}_\mu dS_y + \boldsymbol{h}_\mu dS_z + \iint_\Omega \boldsymbol{S} d\Omega \tag{8}$$

where, Ω is the control volume and $\boldsymbol{S}$ is the boundary surface. The vector $\boldsymbol{W}$ contains the conservative variables.

$$\boldsymbol{W} = \{\rho, \rho u, \rho v, \rho w, \rho E, \rho k, \rho\omega\}^T \tag{9}$$

where ρ is the fluid density, u, v, and w are the three Cartesian velocity components. E is the flow specific total energy. k and ω are the turbulent kinetic and specific dissipation rate.

The flux tensors $\boldsymbol{f}$, $\boldsymbol{g}$, $\boldsymbol{h}$ and $\boldsymbol{f_\mu}$, $\boldsymbol{g_\mu}$, $\boldsymbol{h_\mu}$ in Eq. (8) represent the inviscid convective fluxes and the diffusive fluxes, respectively. The convective fluxes $\boldsymbol{f}$, $\boldsymbol{g}$ and $\boldsymbol{h}$ are defined in terms of the relative velocity $\boldsymbol{u} - \boldsymbol{u_b}$ are

$$\boldsymbol{f} = \Big\{ \rho(\boldsymbol{u}-\boldsymbol{u_b}),\quad \rho u(\boldsymbol{u}-\boldsymbol{u_b}) + p,\quad \rho v(\boldsymbol{u}-\boldsymbol{u_b}), \rho w(\boldsymbol{u}-\boldsymbol{u_b}),\ \rho\Big(E+\frac{p}{\rho}\Big)(\boldsymbol{u}-\boldsymbol{u_b}),\quad \rho k(\boldsymbol{u}-\boldsymbol{u_b}),\quad \rho\omega(\boldsymbol{u}-\boldsymbol{u_b}) \Big\}^T \tag{10}$$

$$\boldsymbol{g} = \Big\{ \rho(\boldsymbol{v}-\boldsymbol{v_b}),\quad \rho u(\boldsymbol{v}-\boldsymbol{v_b}),\quad \rho v(\boldsymbol{v}-\boldsymbol{v_b}) + p,\quad \rho w(\boldsymbol{v}-\boldsymbol{v_b}), \rho\Big(E+\frac{p}{\rho}\Big)(\boldsymbol{v}-\boldsymbol{v_b}), \rho k(\boldsymbol{v}-\boldsymbol{v_b}), \rho\omega(\boldsymbol{v}-\boldsymbol{v_b}) \Big\}^T \tag{11}$$

$$\boldsymbol{h} = \Big\{ \rho(\boldsymbol{w}-\boldsymbol{w_b}),\quad \rho u(\boldsymbol{w}-\boldsymbol{w_b}), \rho v(\boldsymbol{w}-\boldsymbol{w_b}), \rho w(\boldsymbol{w}-\boldsymbol{w_b}) + p,\ \rho\Big(E+\frac{p}{\rho}\Big)(\boldsymbol{w}-\boldsymbol{w_b}), \rho k(\boldsymbol{w}-\boldsymbol{w_b}), \rho\omega(\boldsymbol{w}-\boldsymbol{w_b}) \Big\}^T \tag{12}$$

where $\boldsymbol{u_b} = (u_b, v_b, w_b)^T$ is the grid velocity vector. The diffusive fluxes $\boldsymbol{f}_\mu$, $\boldsymbol{g}_\mu$ and $\boldsymbol{h}_\mu$ due to the viscous shear stresses, thermal diffusion and turbulence diffusion can be written as

$$\boldsymbol{f_\mu} = \Big\{0,\quad \tau_{xx},\quad \tau_{yx},\quad \tau_{zx},\quad u\tau_{xx},\quad +v\tau_{xy}+w\tau_{xz}-q_x,\quad \mu^*\frac{\partial k}{\partial x},\quad \mu^*\frac{\partial\omega}{\partial x}\Big\}^T \tag{13}$$

$$\boldsymbol{g_\mu} = \Big\{0,\quad \tau_{xy},\quad \tau_{yy},\quad \tau_{zy},\quad u\tau_{yx},\quad +v\tau_{yy}+w\tau_{yz}-q_y,\quad \mu^*\frac{\partial k}{\partial y},\quad \mu^*\frac{\partial\omega}{\partial y}\Big\}^T \tag{14}$$

$$\boldsymbol{h_\mu} = \Big\{0,\quad \tau_{xz},\quad \tau_{yz},\quad \tau_{zz},\quad u\tau_{zx},\quad +v\tau_{zy}+w\tau_{zz}-q_z,\quad \mu^*\frac{\partial k}{\partial z},\quad \mu^*\frac{\partial\omega}{\partial z}\Big\}^T \tag{15}$$

where

$$\mu^* = \mu_L + \sigma^*\mu_T \tag{16}$$

where μ_L is the laminar viscosity, μ_T is the turbulent eddy viscosity, σ^* is the turbulent closure constant equal to 0.5, and $\tau_{\alpha\beta}$ with $\alpha, \beta \in \{x, y, z\}$ is the stress tensor expressed as

$$\tau_{\alpha\beta} = \mu\Big(\partial_\alpha u_\beta + \partial_\beta u_\alpha\Big) - \frac{2}{3}\mu\delta_{\alpha\beta}\partial_\alpha u_\beta \tag{17}$$

and

$$q_\alpha = -k\partial_\alpha\Theta \tag{18}$$

In the above equations, μ represents the dynamic viscosity, k is the thermal conductivity, and Θ the temperature. The stress tensor $\tau_{\alpha\beta}$ is the general form of the shear stresses in $\boldsymbol{f}\mu$, $\boldsymbol{g}\mu$ and $\boldsymbol{h}\mu$.

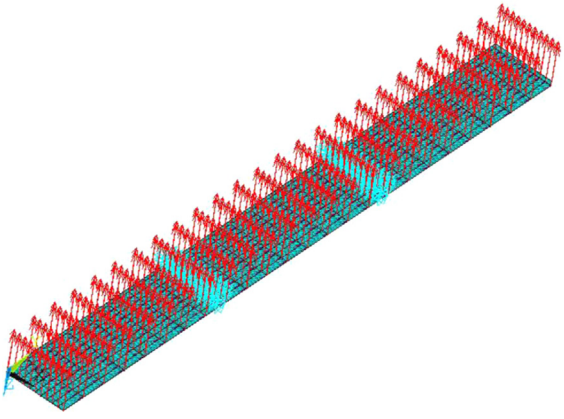

Fig. 5. Diagrammatic sketch for external loads (red arrow) and constrains (cyan arrow) conditions at each cell for ANSYS structural solver.

The source term $\boldsymbol{S}$ is defined as

$$\boldsymbol{S}=\left\{0,\quad 0,\quad 0,\quad 0,\quad 0,\quad \tau_{\alpha\beta}\frac{\partial u_\alpha}{\partial x_\beta}-b^*\rho\omega k,\quad \frac{a\omega}{k}\tau_{\alpha\beta}\frac{\partial u_\alpha}{\partial x_\beta}-b\rho\omega^2\right\}^T \tag{19}$$

with closure constants of $a=5/9$, $b=0.075$, and $b^*=0.09$.

The fluid governing equations could be discretized into the following semi-discrete form

$$\frac{d\boldsymbol{w}}{dt}+\boldsymbol{R}(\boldsymbol{w})=0 \tag{20}$$

where $\boldsymbol{R}$ is the residuals vector. Finite volume approach is used for the spatial discretization in the above equations. A second order artificial and matrix dissipation scheme have been applied for the discretization of the diffusive fluxes. A cell centred finite-volume method has been applied, with the enhanced numerical stability by residual smoothing. A k-ω turbulence model has been applied for the modelling of the high Re of VAT. A grid-deformation algorithm Trans-Finite Interpolation (TFI) has been developed to interpolate the deformation of the structural boundaries onto the flow grid. The cell-centred based method is used to calculate gradients. The discretization of the convective fluxes is based on a second order Roe's flux-difference splitting scheme for Navier-Stokes equations.

2.2.2. Structural dynamics

The structure elastic equations could be discretized in a finite-element model as follows:

$$[M]\ddot{\boldsymbol{x}}_{\boldsymbol{s}}+[C]\dot{\boldsymbol{x}}_{\boldsymbol{s}}+[K]\boldsymbol{x}_{\boldsymbol{s}}=\boldsymbol{F} \tag{21}$$

where $[M]$ denotes the mass matrix, $[C]$ represents the structural damping matrix, $[K]$ is the stiffness matrix and $\boldsymbol{F}$ is total force acting on the blade with equation of $\boldsymbol{F}=F_{ft}=F_f+F_c$. We discretize Eq. (21) by model analysis method using commercial software ANSYS 15.0. After finding the mode shape$[\Phi]$, the following equation could be defined as

$$\boldsymbol{x}_{\boldsymbol{s}}=[\tilde{\Phi}]\boldsymbol{q} \tag{22}$$

where $\boldsymbol{q}$ is the vector of the generalized displacement. Eq. (21) could be premultiplied by the transpose mode shape $[\tilde{\Phi}]^T$. The jth equations are shown as:

$$\ddot{q}_j+2\zeta_j\omega_j\dot{q}_j+\omega_j^2q_j=\frac{\tilde{\varphi}_j}{m_j}F \tag{23}$$

where ζ_j is the modal damping ratio, ω_j is the natural frequency, and m_j is the mass matrix in the jth diagonal element. The above equation could be further discretized by the pseudo-time t^* as

$$\frac{d\boldsymbol{z}_{\boldsymbol{j}}^{\boldsymbol{n}+1}}{dt^*}+\boldsymbol{R}_{\boldsymbol{s}}^*\left(\boldsymbol{z}_{\boldsymbol{j}}^{\boldsymbol{n}+1}\right)=0 \tag{24}$$

In the present in-house code, Eq. (20) is coupled with Eq. (24). Specifically, the wing displacement data are used by the fluid residual calculation as the flow boundary condition and the fluid parameters used by the structure residual calculation as the hydrodynamic forcing. The detailed fluid-structure coupling algorithm is provided in the following.

2.2.3. Fluid-structure coupling

Present Fluid-Structure-Interaction (FSI) solver uses the spline matrix method to connect fluid mesh and structure mesh. Work conservation law is used to determine the relationship between force acting onto the fluid mesh cells and force acting onto the structure mesh cells. The Constant-Volume-Tetrahedron (CVT) method is used for the coupling between fluid solver and structure solver.

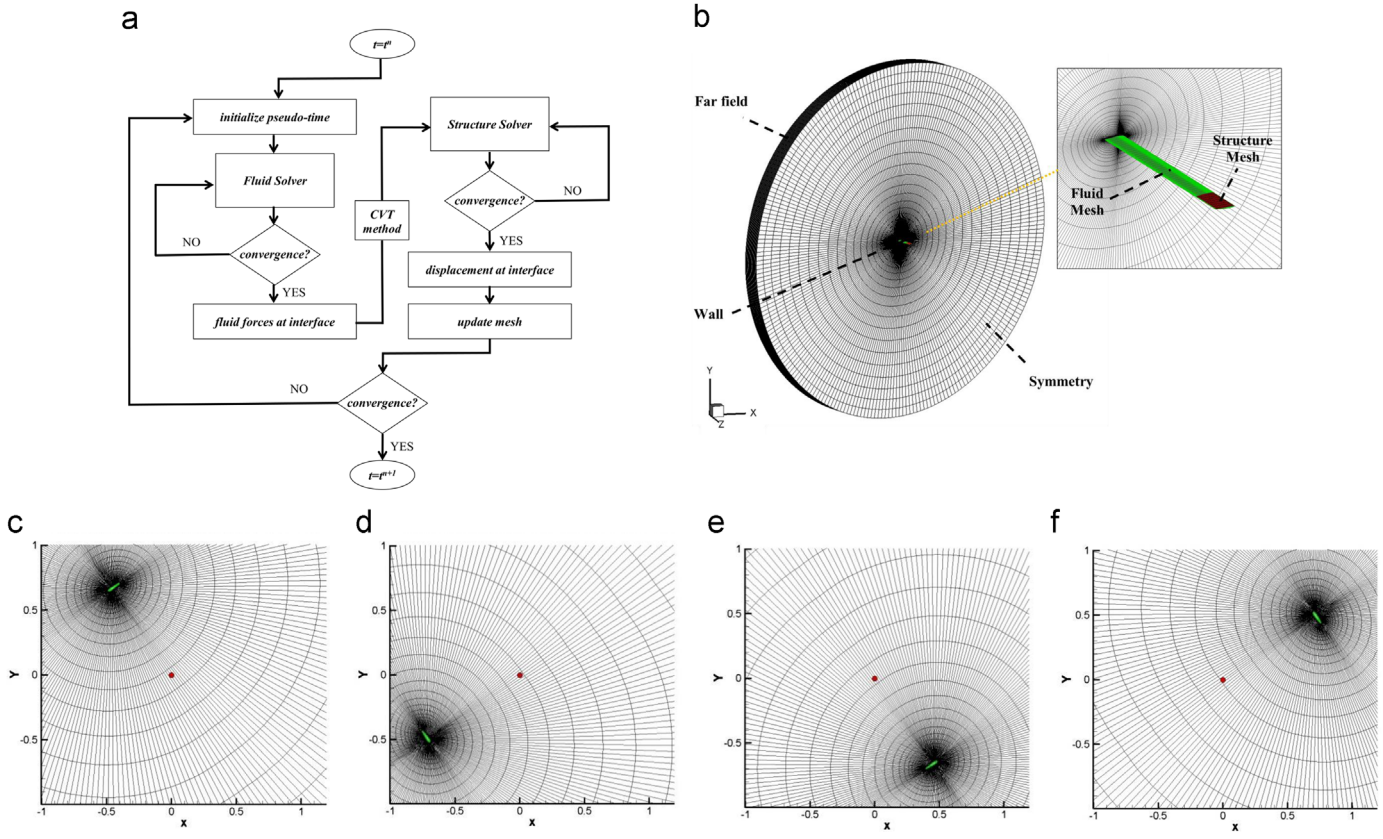

Fig. 6. Flow chart and mesh topology for the present FSI simulation. (a) Flow chart of the present FSI solver. (b) Computational domain.

The detail information of the present FSI solver is described in Xiao and Liao (2010), Xiao et al. (2012), Liu et al. (2013) and Liu et al. (2015).

2.2.4. Stress calculation

Apart from the coupled fluid structure interaction modelling, we also performed the flexible blade stress calculation using commercial software ANSYS. This is used to estimate the maximum displacement and stress distribution when the maximum fluid loads are applied to the blade. The results are compared to those obtained by our in-house code as a part of CFD verification, and summarised in Table 3. A diagrammatic sketch for fluid loads and structural constrains at each cell using ANSYS solver is shown in Fig. 5. As it is seen, uniformly distributed external loads are applied to each structural cell with red arrows. Different constrains which represent the strut locations are indicated as cyan arrows. Hameed and Afaq (2013) tested the effect of the element type on the prediction of maximum stress and deflection of a vertical axis turbine blade. They found that "*The solid45 element type can approximate the large distortion in the shape of the blade*" (Hameed and Afaq, 2013). As we adopt a similar turbine blade model and strut locations to that of Hameed and Afaq's work, SOLID45 element is selected for our Finite Element Analysis.

In order to compare the structural stress for various types of blades discussed in this study, non-dimensionalized stress c_{st} is introduced and defined as:

$$c_{st} = \frac{\sigma}{\frac{1}{2}\rho_f U^2} \tag{25}$$

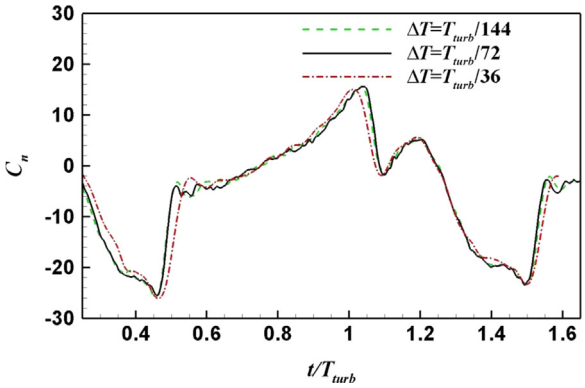

Fig. 7. Sensitivity study of time step size.

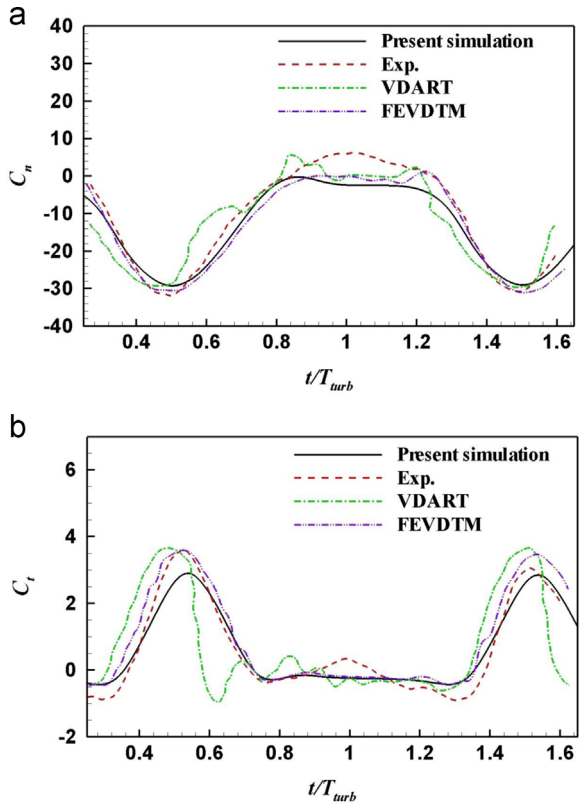

Fig. 8. Validation results for a rigid blade turbine-comparison with towing tank data (Exp.) by Strickland et al. (1980), Free Vortex Model (VDART) by Strickland et al. (1979) and Vortex method combined with finite element analysis (FEVDTM) by Ponta and Jacovkis (2001). (a) Instantaneous normal force coefficient. (b) Instantaneous thrust coefficient.

Table 2
Case summary for the present simulation.

case group	Π	l_{st}/c	λ
Rigid	∞	–	3.50–7.50
Flexible blade with middle strut	3.19E+03	$\frac{10}{3}$	3.50–7.50
High flexibility blade with middle strut	9.37E+02	$\frac{10}{3}$	3.50–7.50
Flexible blade with tip strut	3.19E+03	0	3.50–7.50

2.2.5. Numerical issues

Fig. 6(b) shows the computational domain and mesh for both the fluid and the blade structure. The model size in span wise direction is 10*c*. The blade is set to be 50*c* away from the incoming flow and outflow boundaries. Far field boundary condition is applied to the inlet and outlet boundaries with uniform constant velocity in *x* axis direction. High mesh density has been used around the blade to enhance the calculation accuracy under high *Re* condition. The turbine blade is located in the centre of the fluid grid. There is a rotation motion around the rotation centre for the fluid mesh to represent the rotation motion of the turbine blade during the calculation. The distance between the turbine blade (mesh centre) and the rotation centre is one turbine radius (R). Fig. 6 (c) - (f) shows the mesh movement during one turbine revolution at different time instants. The sensitivity study of time step size is performed at tip speed ratio $\lambda=3.5$ and the predicted results are shown in Fig. 7. It is seen that there is no significant difference between time step of $T_{turb}/144$ and $T_{turb}/72$. Considering a reasonable calculation time, $T_{turb}/72$ is selected for the following calculation.

2.3. Validations and verifications

Our present FSI code has been extensively validated in our previous publications (see Xiao and Liao, 2010; Xiao et al., 2012 and Liu et al., 2013). The fluid structure interaction part is also validated in Liu et al. (2015). In the present study, further investigations on a three-dimensional vertical axis turbine with rigid blade have been conducted. The results predicted by our numerical model are compared with the results by Strickland et al. (1980), Strickland et al. (1979) and Ponta and Jacovkis (2001) in Fig. 8. Good agreement is shown for this case. A convergence test for the ANSYS Finite Element Analysis has also been carried out for the case of $\lambda=5.5$, $\Pi=3.19\times10^3$ and $l_{st}/c=10/3$. By doubling the calculation element numbers, the difference of maximum deflection and stress between fewer elements and more elements results are all smaller than 0.15%, which passes the FEA convergence criteria.

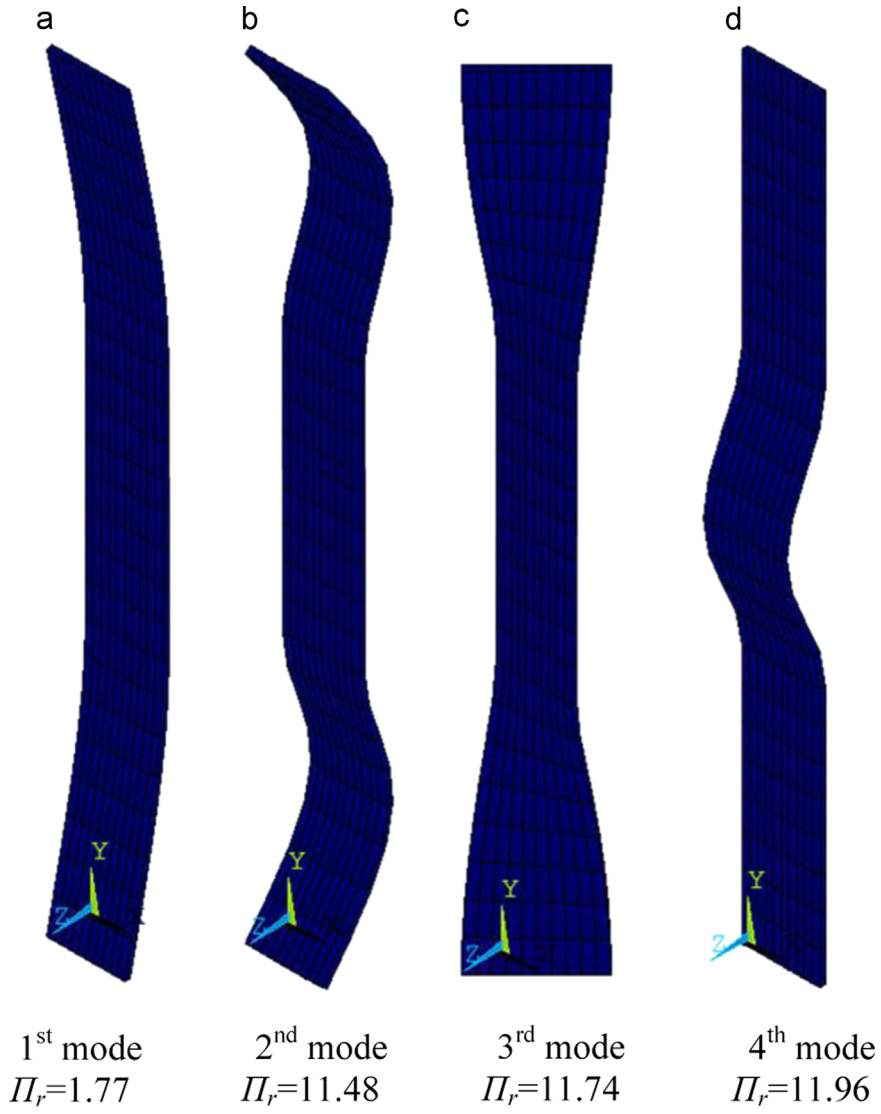

Fig. 9. First four mode shapes with $l_{st}/c=\frac{10}{3}$, $\Pi = 3.19 \times 10^3$.

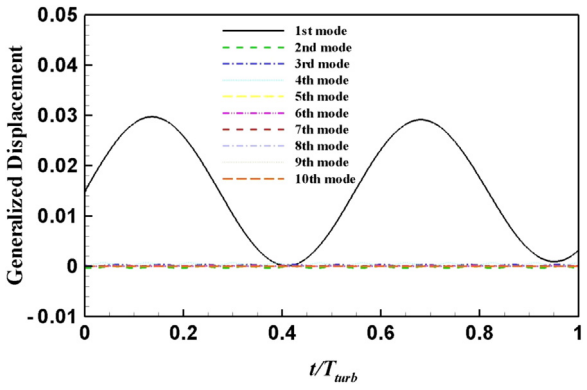

Fig. 10. Time histories of the generalized displacements of first ten modes with $l_{st}/c=\frac{10}{3}$, $\Pi = 3.19 \times 10^3$ and $\lambda=5.5$.

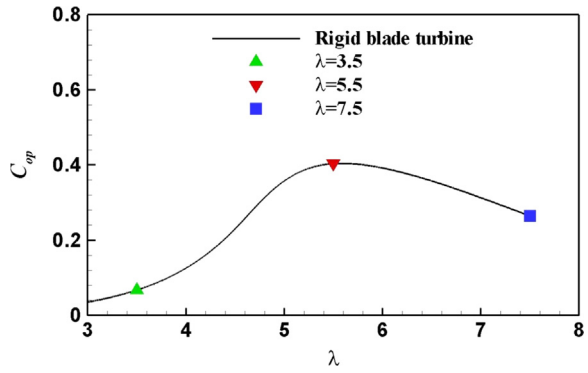

Fig. 11. Power coefficient v.s. tip speed ratio for rigid blade turbine and c_{op} value for $\lambda=3.5$, 5.5 and 7.5.

3. Results

As stated in Section 2.1, we start our investigation on a flexible blade of an effective stiffness $\Pi=3.19 \times 10^3$ and strut location $l_{st}/c=10/3$. The predicted blade structural characteristics (blade deformation and structure stress) and external loads are examined and compared with a rigid blade in Sections 3.1 and 3.2. Sections 3.3–3.5 are the flexibility effect, strut effect and energy extraction performance of turbine, respectively. A summary of relevant cases are listed in Table 2. For a rigid blade, we assume it has an infinite large stiffness. To carry on an FSI study, modal analysis method is used. First ten natural vibrational modes are adopted to estimate the blade deflections. First four mode shapes and their frequency ratios for $l_{st}/c=10/3$ and $\Pi=3.19 \times 10^3$ are shown in Fig. 9 as an example. These four

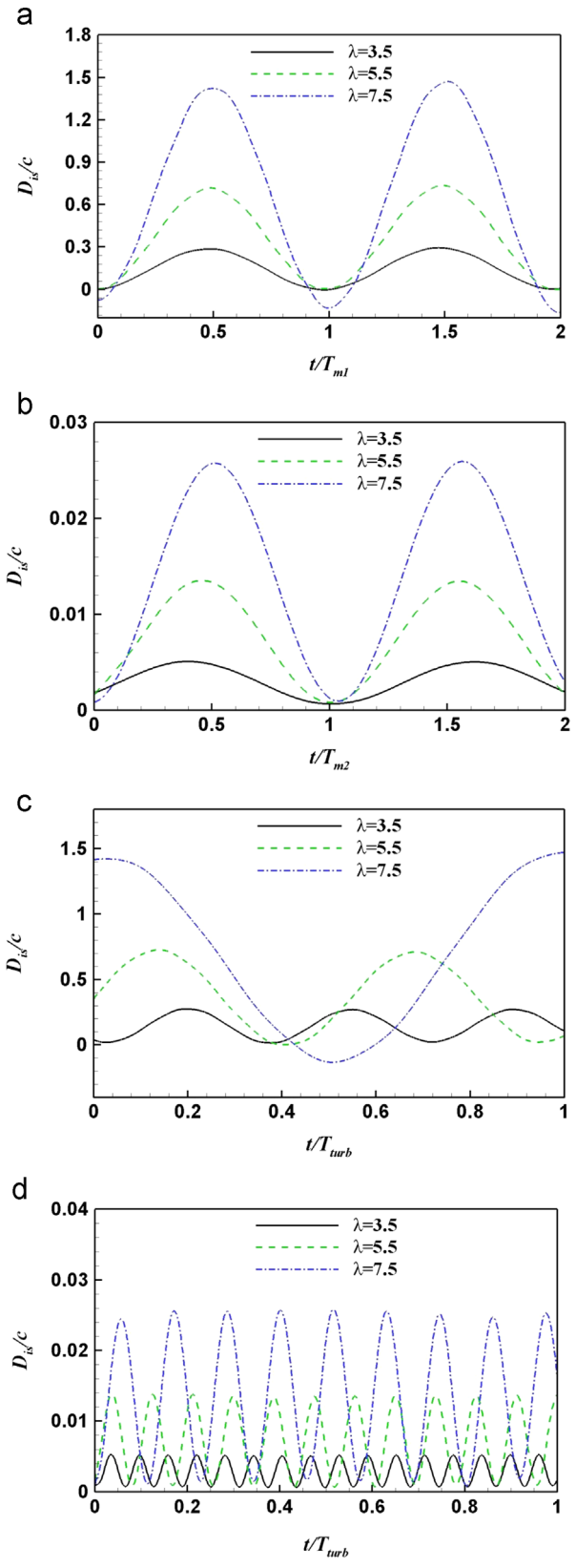

Fig. 12. Instantaneous non-dimensionalize displacement for different tip speed ratios with $l_{st}/c=\frac{10}{3}$, $\Pi=3.19\times10^3$. (a) and (c) $H/c=0$ and (b) and (d) $H/c=5$ (a) and (b) time is non-dimensionalized by blade mode periods and (c) and (d) time is non-dimensionalized by turbine revolution. (a) H/c=0. (b) H/c=5. (c) $H/c=0$. (d) $H/c=5$.

modes are identified as the first bending mode for region a and c ($1/T_{m1}$), the second bending mode for region a and c ($1/T_{m7}$), first torsion mode for region a and c ($1/T_{m3}$) and the first bending mode for region b ($1/T_{m2}$) (see Fig. 4(b) for the definitions of regions a to c). The generalized displacement q_j (as indicated in Eqs. (22) and (23) variation for the first ten modes at $\lambda=5.5$ during one revolution is shown in Fig. 10. Clearly seen from this figure is that the first mode plays a leading role on the blade structural deformation behaviour.

3.1. Structure characteristics

In this section, we focus our study on three typical tip speed ratios, i.e. $\lambda=3.5$, 5.5 and 7.5. They are selected to represent three statuses for power coefficient c_{op} vs. λ, i.e. climbing up ($\lambda=3.5$), peak c_{op} ($\lambda=5.5$) and drop down ($\lambda=7.5$) as indicated in Fig.11.

Fig. 12 shows the instantaneous non-dimensionalized bending displacement D_{is}/c for different tip speed ratios λ with $l_{st}/c=10/3$ and $\Pi=3.19\times10^3$ at the blade tip ($H/c=0$) and centre (i.e. $H/c=5$). Two time periods are used to non-dimensionalize the time, i.e. turbine revolution period (T_{turb}) and the 1st mode shape period of region a (or region c) and b (T_{m1} and T_{m2}). The positive direction of the displacement D_{is}/c is aligning with the positive y_l axis at local body fitted coordinate (see Fig. 2). Based on these results, it is obvious that the flexible blade deforms periodically with one dominant frequency under various tip speed ratios λ and at different H/c. Given a large λ condition, the blade displacement is getting larger because of the increased centrifugal force at a large rotating speed. In addition, the flexible blade always shows a larger deformation at tip ($H/c=0$) than at its centre ($H/c=5$) for this middle struts support (see Fig. 4(b)). For example, at $\lambda=5.5$, the displacement at blade tip is 7.26×10^{-1} which is 55.85 times larger than that at the blade center. A further examination on these plots shows that all deformations display a positive magnitude, pointing to the positive y_l. Thus, it is inferred that the flexible deformation is mainly induced by the large magnitude of centrifugal force (c_c) rather than the fluid forces as shown in Fig. 3. A careful look at Fig. 12 (a) and (b), where the time history of deformation is represented against the instantaneous time relative to the 1st bending mode period of region a ($\Pi_r=1.77$) and b ($\Pi_r=11.96$), indicates that the structural deformation frequency matches exactly the system natural frequency.

Fig. 13 plots the instantaneous blade twist angle at the tip and centre of blade for different tip speed ratios λ. The blade twist angle is defined as the nose up positive. A similar behaviour as the bending effect discussed above is observed. In fact, the twist angles tend to behave like a sinusoidal motion under different λ and H/c conditions with positive values. The increase of the tip speed ratio results in an increase of the twist angle at both blade tip and center. The maximum twist angle at blade tip is no more than 2.23°, while at blade center it is less than 0.40°. The mechanism associated with twist motion will be discussed in Section 3.2.

To further analyse the structural deformation along blade spanwise direction, Fig. 14 plots the bending and twist displacement contour under $l_{st}/c=10/3$, $\Pi=3.19\times10^3$ and $\lambda=5.5$ conditions at four different time instants during one cycle. It is apparent that the large deflection occurs near the vicinity of blade free ends, i.e. H/c between 0 to 0.5 and H/c between 9.5 to 10. Because of the support of two struts, the central part of region b has the minimum deformation as compared to regions a and c. This trend is observed at all instantaneous time during one cycle. The twist behaviour could also be observed at time instant $t/T_{turb}=7/8$ at region a, b and c in Fig. 14, (as indicated by the inclined contour lines). An

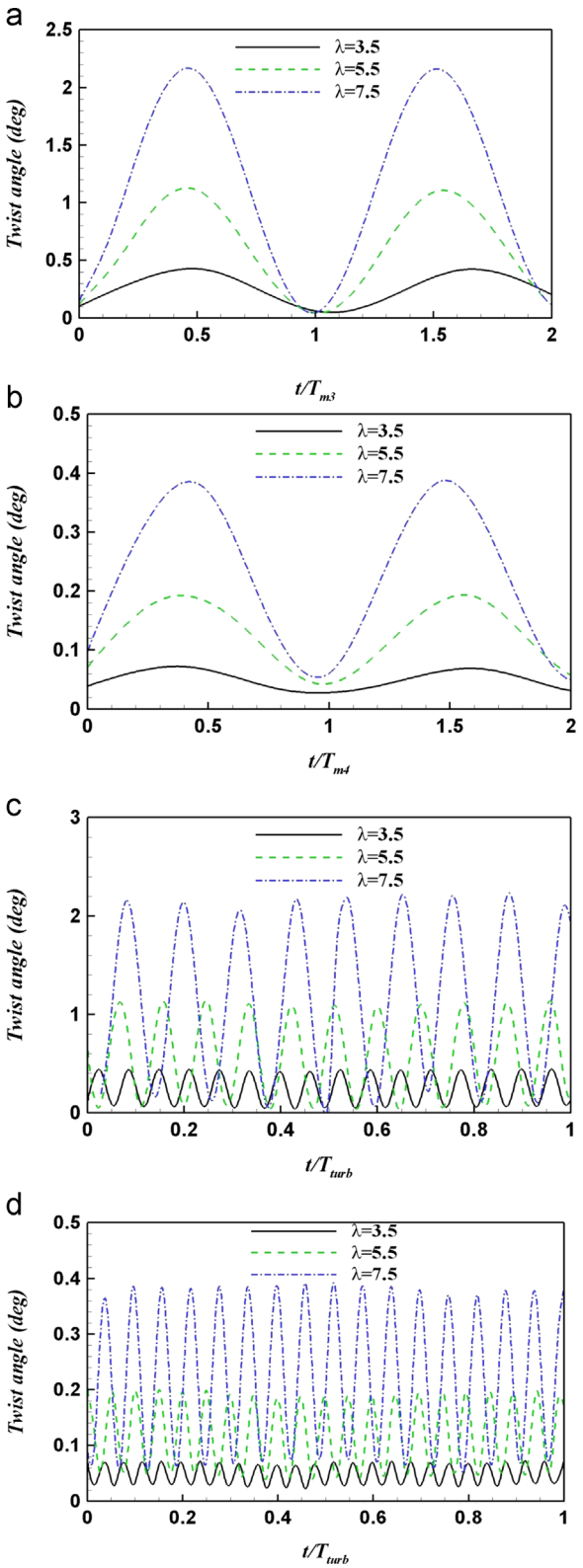

Fig. 13. Instantaneous twist angle for different tip speed ratios with $l_{st}/c=\frac{10}{3}$, $\Pi=3.19\times10^3$. (a) and (c) $H/c=0$ and (b) and (b) $H/c=5$ (a) and (b) time is non-dimensionalized by blade mode periods and (c) and (d) time is non-dimensionalized by turbine revolution. (a) $H/c=0$. (b) $H/c=5$. (c) $H/c=0$. (d) $H/c=5$.

increase of tip speed ratio leads to an increased deformation as shown from Fig. 15 for $\lambda=7.5$.

In order to further analyse the flexible blade structural stress, we adopt ANSYS structural solver (as mentioned in Section 2.1.1)

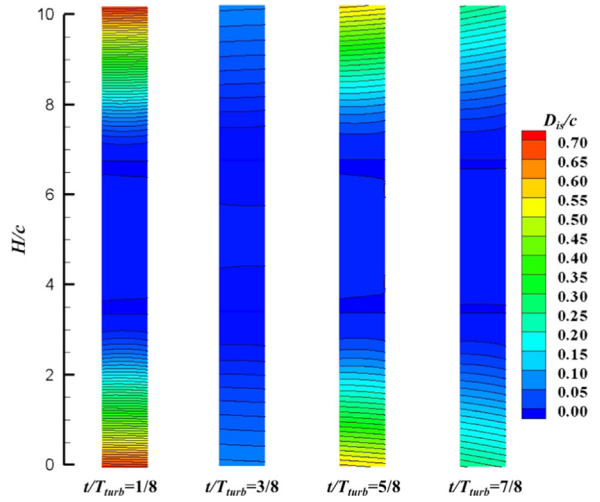

Fig. 14. Non-dimensionalized bending and twist displacement contour with $l_{st}/c=\frac{10}{3}$, $\Pi=3.19\times10^3$ and $\lambda=5.5$ viewing from the inner side of blade.

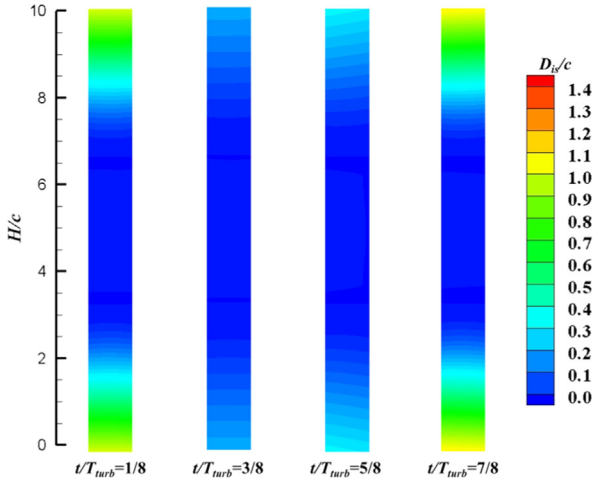

Fig. 15. Non-dimensionalized bending and twist displacement contour with $l_{st}/c=\frac{10}{3}$, $\Pi=3.19\times10^3$ and $\lambda=7.5$ viewing from the inner side of blade.

Table 3
Comparison for the maximum displacement ratio and stress coefficient.

case type				*max.* D_{is}/c		*max.* c_{st}
Data source	l_{st}/c	Π	λ	**in-house FSI solver**	**ANSYS**	**ANSYS**
Hameed and Afaq (2013)	0.217	2.81E+05	4.1	–	3.85E−02	2.87E+06
The present research	10/3	3.19E+03	5.5	7.26E−01	6.63E−01	1.48E+06
			6.5	1.15E+00	9.77E-01	2.18E+06
			7.5	1.53E+00	1.33E+00	2.96E+06
		9.37E+02	5.5	1.76E+00	1.74E+00	2.57E+06
	0	3.19E+03	5.5	6.17E-01	6.20E-01	1.30E+06

to estimate the deflections and stresses under the extreme condition, where the flexible blade endures the maximum external loads. Results are summarised in Table 3 along with the data from Hameed and Afaq (2013). By comparing the results obtained by various methods, it is observed that the prediction of maximum displacement from ANSYS solver has a slight discrepancy from the results estimated by the present in-house code. One possible

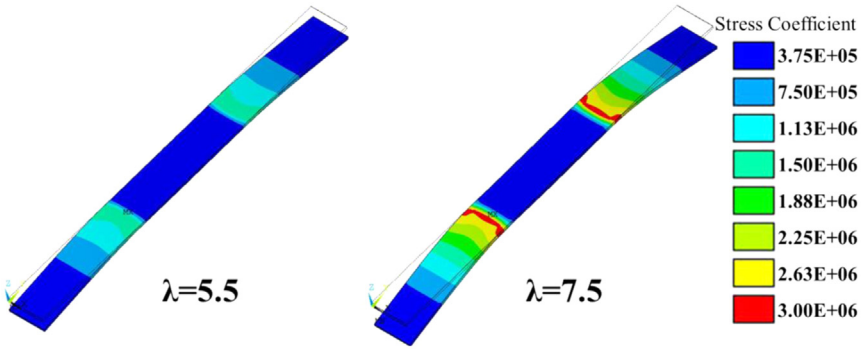

Fig. 16. Contour of stress distribution over the blade under the largest external load condition for the flexible blade for different tip speed ratio with $l_{st}/c=\frac{10}{3}$ and $\Pi=3.19\times10^3$ viewing from the inner side of blade.

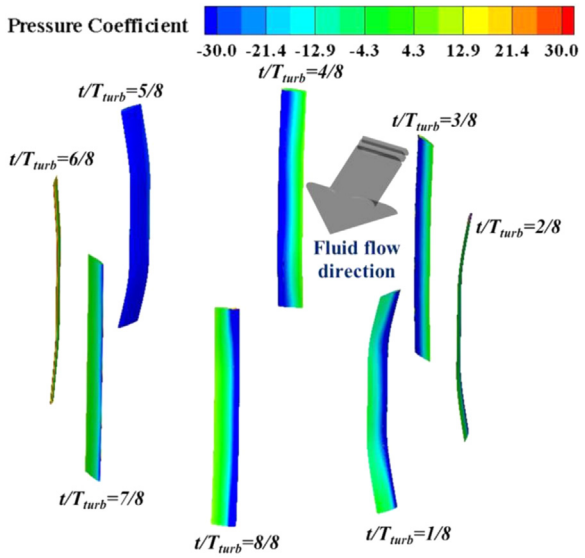

Fig. 17. Blade bend-twist motion and pressure distribution for different time instants with $l_{st}/c=\frac{10}{3}$, $\Pi=3.19\times10^3$ and $\lambda=5.5$.

explanation may due to the simplified models are assumed in ANSYS structural solver, such as a uniformly distributed loading applied on the blade. The general trend of maximum displacement and stress variation with tip speed ratio is consistent, i.e. both increase with the growing of λ. The stress distribution contour from ANSYS solver at $\lambda=5.5$ and $\lambda=7.5$ are plotted in Fig. 16. It is clearly shown that the regions a and c endure more stress than region b. The maximum stress appears near the strut location.

3.2. External loads

In order to explain the structure characteristics observed in Section 3.1, an analysis of the fluid loads onto the turbine blade is carried out in this section. Fig. 3 shows the time history of forces applied on the blade during one cycle at two tip speed ratios, i.e. $\lambda=5.5$ and $\lambda=7.5$. As discussed in Section 2.1, the external loads acting on the blade (F_{ft}) can be decomposed into the centrifugal force (F_c) and fluid load (F_f), which can be non-dimensionalized and represented by the centrifugal force coefficient (c_c) and fluid force coefficient (c_f), respectively. The dynamic displacement of blade motion (bending or twist) is dictated by this net/resultant force ($c_{ft}=c_c+c_f$). During one revolution, apparently, centrifugal force (c_c) does not change its magnitude and always points to blade external normal direction (see Fig. 2). However, the fluid force (c_f), which is mainly contributed from the net pressure force acting on the blade, varies dramatically in its direction and magnitude within one cycle as clearly depicted in Fig. 3(a) and (b). In addition, the variation trend of c_f against time is also tip speed ratio dependent. Under various flow and structure conditions studied herein, we found that the centrifugal force coefficient (c_c) is always larger than fluid force coefficient (c_f). At some time intervals within one cycle, they may point to the same direction (exterior normal), while at other intervals, they have opposite direction. With this in mind, it is obvious that, the blade bending direction is always outwards as displayed in Figs. 11, 12 and 17. The dynamic behaviour of deflection motion is mainly determined by the fluid loads (c_f) or net pressure we will discuss shortly.

The pressure distribution on the blade is examined herein to aid our above force analysis. Fig. 17 plots blade bending and twist motion contour and their pressure distribution at different time instants within one cycle. It is observed that the blade deflection is getting larger when the net pressure loads acting on the blade having a small value. Two time instants with a small and large deflection are selected for a further analysis shown in Fig. 18, where a detail comparison between flexible and rigid blade at both inner and outer sides of blade are presented. The pressure coefficient c_{pr} plot at $H/c=0$ and $H/c=5$ are displayed in Fig. 19. At $t/T_{turb}=3/8$ when the blade deflection is small, it is obvious that no apparent difference exists of pressure distribution for a flexible and a rigid blade at both sides. In addition, the net pressure load is high as compared to the time instant of $t/T_{turb}=5/8$ causing a small total force (c_f) and thus a small blade deformation. However, at $t/T_{turb}=5/8$ when the flexible blade reaches to a large deflection shown in Fig. 18(b), the pressure loads acting on a flexible blade is lower than that of the rigid blade. From Fig. 19(b), the c_{pr} has a significant decrease at both inner and outer sides with a flexible blade. Moreover, the decrease of c_{pr} at blade outer side is much larger than that of inner side, leading to a decrease of the net pressure loads. Refer to Fig. 3(b), Fig. 19(a) and (b), since the net pressure loads are all negative at both $t/T_{turb}=3/8$ and $t/T_{turb}=5/8$, thus c_f and c_c counteracts with each other. Therefore, at $t/T_{turb}=5/8$, a larger total force c_{ft} and larger outward bending motion of the blade are observed.

The Leading Edge Suction (LES) effect is an important phenomena which influences the fluid flow field and the force generation for airfoil (DeLaurier and Harris, 1982; Chimakurthi et al., 2009). This phenomena has also been observed in the present study, indicated by the low pressure region at the blade leading edge (shown in Fig. 18(b)) and the suction peak (shown in Fig. 19 (b)). For the flexible blade, the magnitude of LES is lower than rigid blade, but the region which is affected by the LES effect is larger than that of the rigid blade (especially in the chord wise direction). Because of the existence of LES effect, the foil leading edge experiences an additional suction force which generates an extra moment relative to its mass center in $x_lo_ly_l$ plane. This moment leads to a nose up position twist on the blades, which explains the

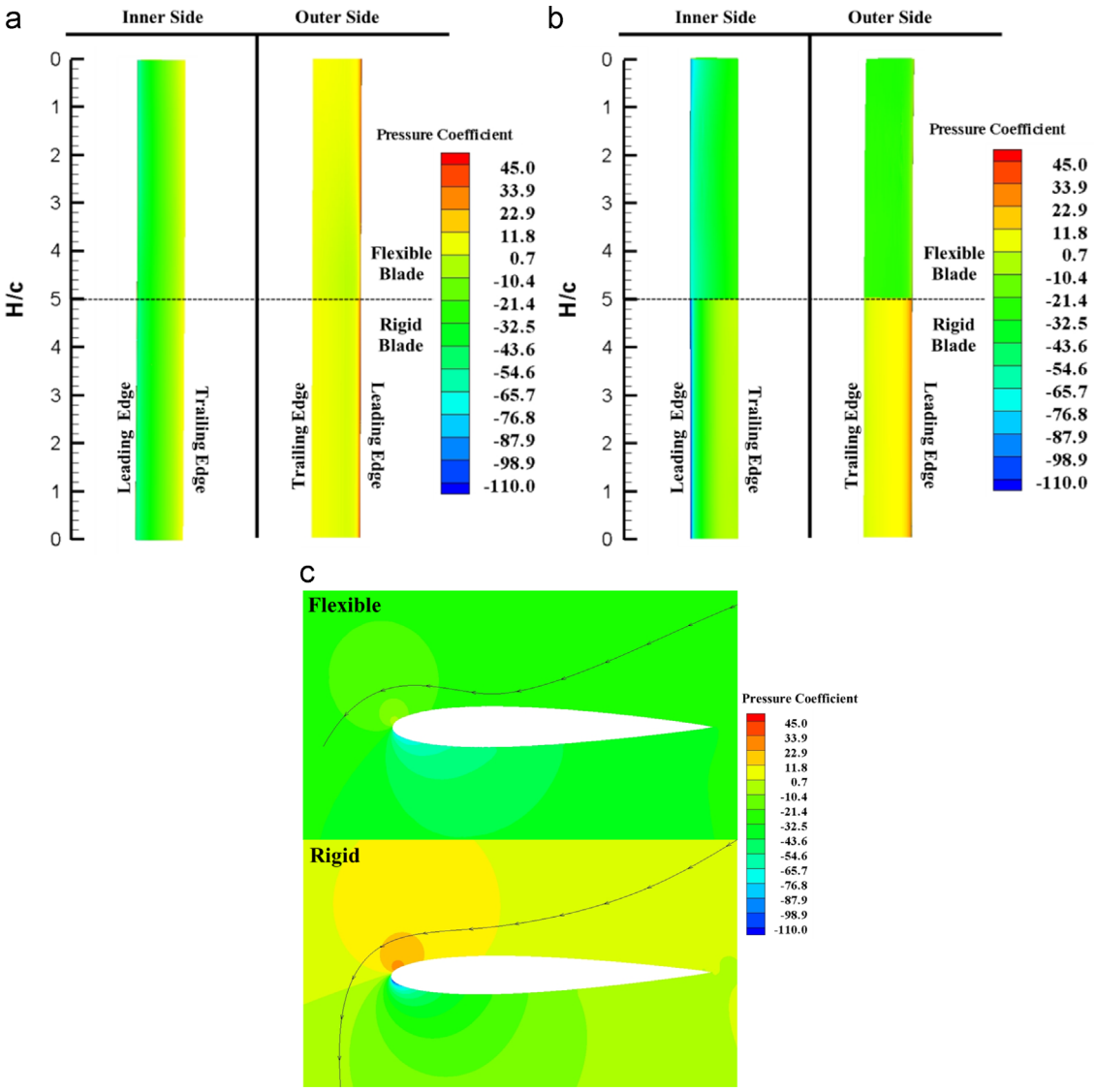

Fig. 18. Pressure distribution with $l_{st}/c=\frac{10}{3}$, $\Pi=3.19\times10^3$ and $\lambda=5.5$. (a) $t/T_{turb}=3/8$ and (b) and (c) $t/T_{turb}=5/8$. (a) Blade pressure distribution at $t/T_{turb}=3/8$ (b) Blade pressure distribution at $t/T_{turb}=5/8$. (c) Pressure distribution around blade at $t/T_{turb}=5/8$.

reason why the blade has the twist motion and the twist angle is always positive as shown in Fig. 13. The pressure contour plots around the blade section shown in Fig. 18(c) coincide with the phenomenon described above.

The λ effect on the pressure distribution is shown in Fig. 20 comparing the flexible blade with $\lambda=5.5$ and $\lambda=7.5$ at the time instant of $t/T_{turb}=5/8$. A large pressure drop with the increase of λ is shown and the LES effect is pronounced at a larger λ.

3.3. Influence of flexible blade stiffness

In this section, a flexible blade with a small effective stiffness Π of 9.37×10^2 under $l_{st}/c=10/3$ condition is tested to study the effect of stiffness on blade structural characteristics.

Figs. 21 and 22 show the bending and twist deflection of this flexible blade. As we can see, by reducing the effective stiffness, the blade flexibility is increased, leading to a profound increase of structural deformation as compared to a less flexible blade in Figs. 13 and 14. In addition, the maximum stress coefficient (c_{st}) is also increased as summarized in Table 3. The stress coefficient contour shown in Fig. 23 indicates the occurrence of a maximum stress around the strut, which is similar to the case of $\Pi=3.19\times10^3$. However, with this more flexible blade, the magnitude of stress is enlarged. The instantaneous blade bend-twist motions and the pressure distribution applied on the blade are shown Fig. 24. Similar to a more rigid blade case, large blade deformation is caused by low pressure acting on the blade. This is well reflected by the pressure distributions plots at $t/T_{turb}=4/8$ and $t/T_{turb}=5/8$ in Fig. 25. In fact, the c_{pr} is around -100 in Fig. 25 (a) for the blade of $\Pi=9.37\times10^2$, which is much lower than the blade of $\Pi=3.19\times10^3$ at $t/T_{turb}=1/8$. However, at $t/T_{turb}=5/8$, as shown in Fig. 25(b), the c_{pr} is around 40, which is higher than the blade with $\Pi=3.19\times10^3$. Under this condition, the blade deforms oppositely with centrifugal force direction. The LES phenomenon is not remarkable for both rigid and flexible blades with different Π because of the small blade instantaneous Angle of Attack (AOA) at these two time instants.

3.4. Influence of two different strut locations

In this section, two different strut locations which connect the flexible blade with radial arms at blade tip (i.e. $l_{st}/c=0$) as seen in Fig. 4(b) is studied to provide some preliminary information of the strut location effect. The comprehensive study of the strut location

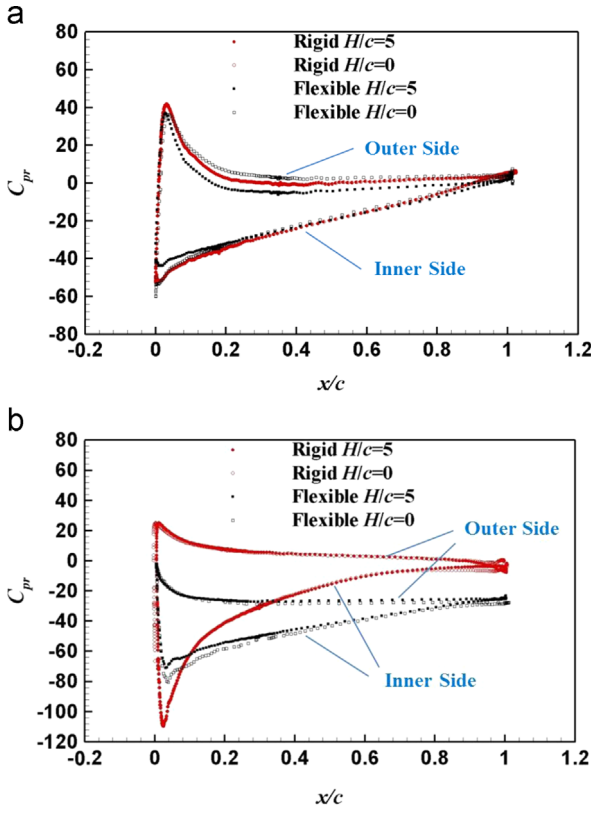

Fig. 19. Pressure coefficient distribution at (a) $t/T_{turb}=3/8$ and (b) $t/T_{turb}=5/8$ with $l_{st}/c=\frac{10}{3}$, $\Pi = 3.19\times10^3$ and $\lambda=5.5$. (a) $t/T_{turb}=3/8$. (b) $t/T_{turb}=5/8$.

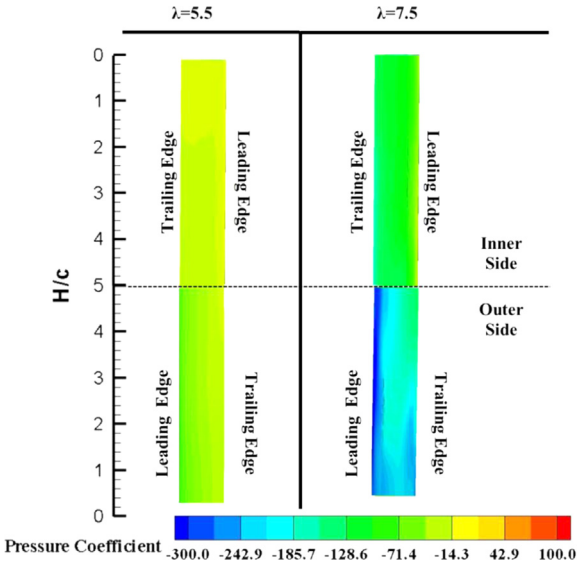

Fig. 20. Pressure distribution at $t/T_{turb}=5/8$ for different tip speed ratios with $l_{st}/c=\frac{10}{3}$ and $\Pi = 3.19\times10^3$.

effect is our current undergoing task, which will be presented in a separate paper. A flexible blade with $\Pi=3.19\times10^3$ is used in this study. As mentioned in Section 2.1, the whole blade could be treated as a simple beam with tip strut support which is expected to show some different structural characteristics and hydrodynamics performances as supported by central struts investigated in the previous sections.

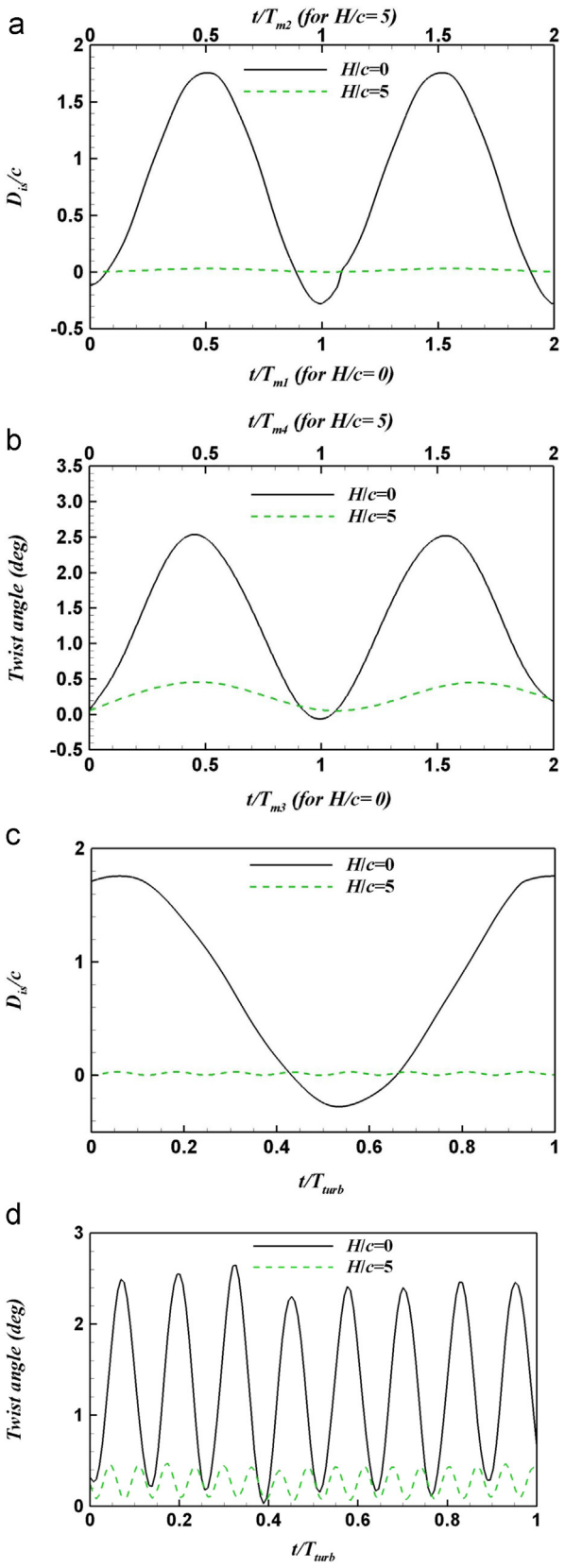

Fig. 21. Structure characteristics with $l_{st}/c=\frac{10}{3}$, $\Pi=9.37\times10^2$ and $\lambda=5.5$. (a) and (b) time is non-dimensionalized by blade mode periods and (c) and (d) time is non-dimensionalized by turbine revolution period. (a) Instantaneous non-dimensionalized displacement. (b) instantaneous twist angle. (c) Instantaneous non-dimensionalized displacement. (d) instantaneous twist angle.

Fig. 26 shows the D_{is}/c and twist angle under $l_{st}/c=0$, $\Pi=3.19\times10^3$ and $\lambda=5.5$. Compared to the results with $l_{st}/c=10/3$, $\Pi=3.19\times10^3$ and $\lambda=5.5$, the maximum D_{is}/c are reduced while the maximum twist angle remains the same. The displacement and twist angle at blade tips are all zero because of the struts, as shown in Figs. 26 and 27. The maximum displacement amplitude occurs at the blade center ($H/c=5$) as can be seen from Fig. 27. A detailed comparison between the condition of $l_{st}/c=0$, and the condition of $l_{st}/c=10/3$, is shown in Table 3. From the stress distribution contour under the largest external load condition in Fig. 28, the maximum stresses exist at blade tips. Though the peak c_{st} has decreased by using tip strut ($l_{st}/c=0$) instead of middle strut ($l_{st}/c=10/3$), a large area having high stress is observed with c_{st} around 7.0×10^5.

The blade bending and twist motion and pressure distribution at different time instants are shown in Fig. 29 which shows the similar observation as previous sections. Pressure distribution at $t/T_{turb}=1/8$ and $t/T_{turb}=4/8$ for both inner side and outer side compared with middle strut blade are displayed in Fig. 30. The LES effect is quite obvious by using tip strut flexible blade in these two plots. It results in a large twist behaviour at $t/T_{turb}=1/8$ and 4/8 as shown in Fig. 26(b).

3.5. Energy extraction

As an energy extraction device, the vertical axis turbine with flexible blade is also investigated on its energy extraction performance in this section. Fig. 31 summarizes the instantaneous moment coefficient (c_m) under three different structural parameters discussed in the above sections along with the rigid blade results. It is seen that the peak c_m enlarges by using a flexible blade and high frequency fluctuations are observed during one revolution, which indicates the appearance of flow field instability. Fig. 32 displays the vorticity field at $t/T_{turb}=5/8$ for

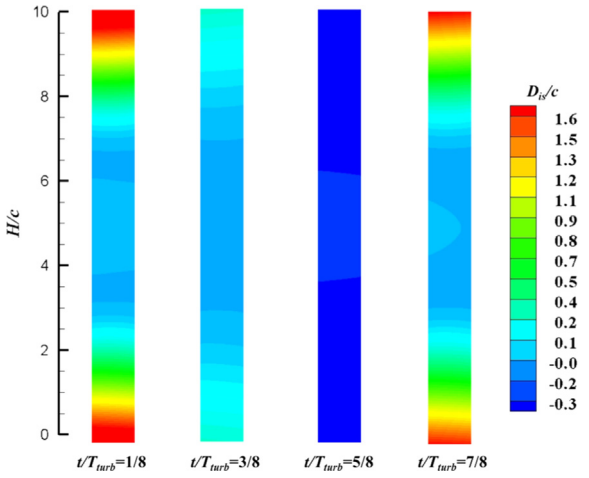

Fig. 22. Non-dimensionalized bending and twist displacement contour with $l_{st}/c=\frac{10}{3}$, $\Pi=9.37\times10^2$ and $\lambda=5.5$ viewing from inner side of blade.

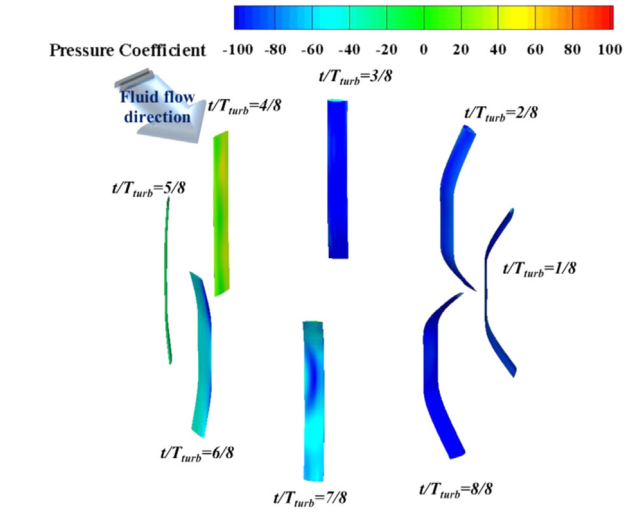

Fig. 24. Blade bend-twist motion and pressure distribution for different time instants with $l_{st}/c=\frac{10}{3}$,$\Pi=9.37\times10^2$ and $\lambda=5.5$.

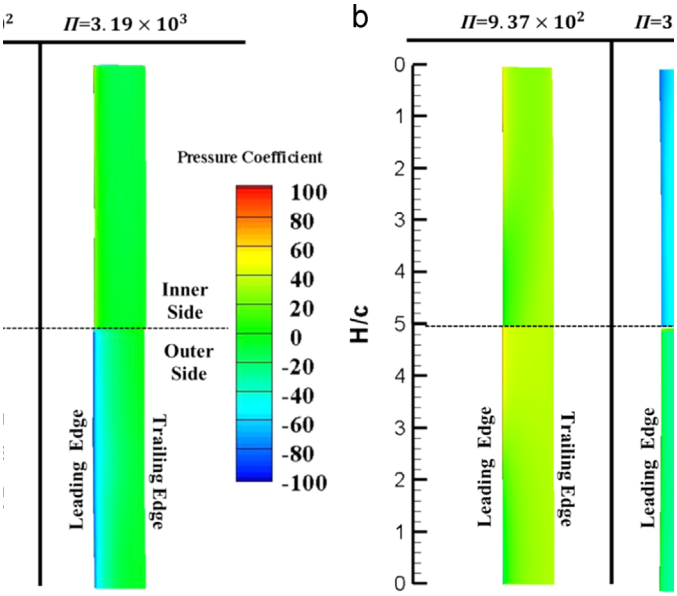

Fig. 25. Pressure distribution at (a) $t/T_{turb}=1/8$ and (b) $t/T_{turb}=5/8$ with $l_{st}/c=\frac{10}{3}$,$\lambda=5.5$ and $\Pi=9.37\times10^2$ compared with $\Pi=3.19\times10^3$. (a) $t/T_{turb}=1/8$ (b) $t/T_{turb}=5/8$.

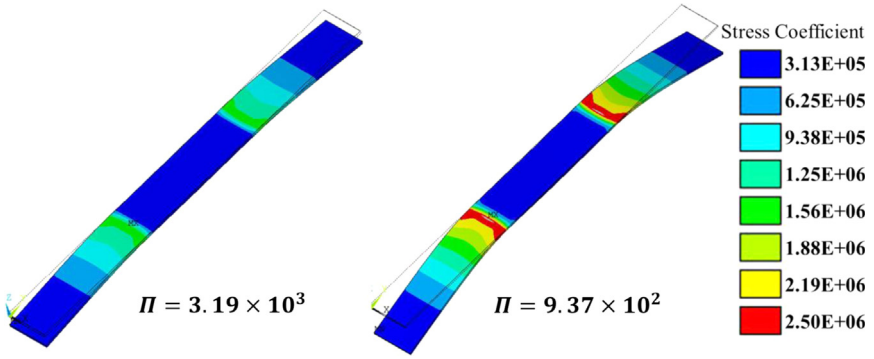

Fig. 23. Contour of stress distribution over the blade under the largest external load condition for the flexible blade with $l_{st}/c=\frac{10}{3}$,$\Pi=9.37\times10^2$ and $\lambda=5.5$ viewing from the inner side of blade.

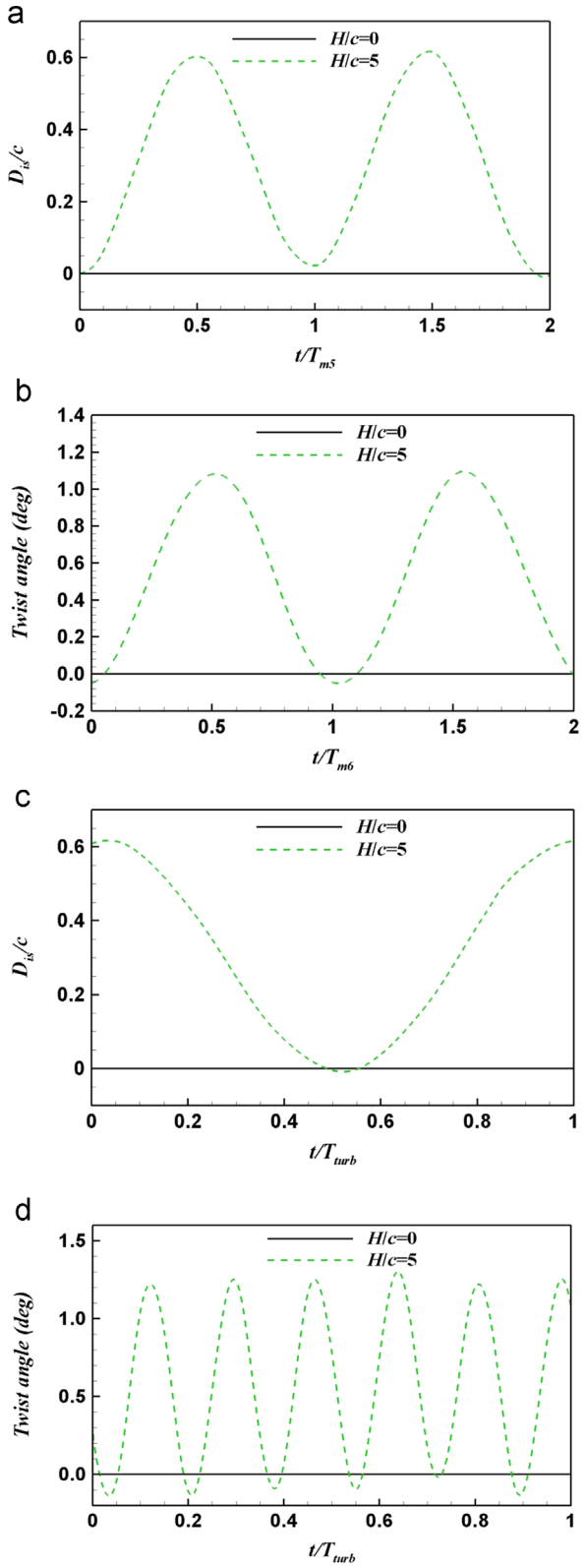

Fig. 26. Structure characteristics with $l_{st}/c=0$, $\Pi=3.19\times10^3$ and $\lambda=5.5$. (a) and (b) time is non-dimensionalized by blade mode periods and (c) and (d) time is non-dimensionalized by turbine revolution. (a) Instantaneous non-dimensionalized displacement. (b) instantaneous twist angle. (c) Instantaneous non-dimensionalized displacement. (d) instantaneous twist angle.

a flexible blade under $l_{st}/c=0$, $\Pi=3.19\times10^3$ and $\lambda=5.5$ condition as compared to a rigid one. A large flow separation is clearly seen associated with a flexible blade as observed in Fig. 31.

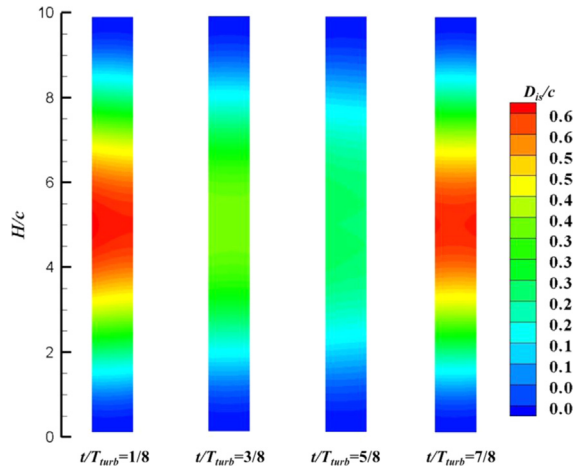

Fig. 27. Non-dimensionalized bending and twist displacement contour with $l_{st}/c=0$, $\Pi=3.19\times10^3$ and $\lambda=5.5$ viewing from the inner side of blade.

The time averaged power coefficient c_{op} variation with λ for both rigid blade and flexible blade turbine under three different conditions are shown in Fig. 33. At the condition of $l_{st}/c=10/3$ and $\Pi=3.19\times10^3$ and when λ is smaller than 6.0, it is observed that the flexible blade could enhance the overall energy performance compared with the rigid blade turbine. An up to 8% enhancement of c_{op} is observed. The tip speed ratio λ, at which the peak c_{op} occurs, can move towards a smaller value. With a further increasing of λ, the energy extraction performance for the flexible blade turbine drops suddenly compared to a rigid blade turbine. In addition, by reducing Π or moving strut to the blade tip ($l_{st}/c=0$), the tip speed ratio (λ) associated with a peak c_{op} moves towards low λ and a smaller c_{op}. However, all of the above discrepancy in c_{op} nearly diminishes when λ is reduced to around 4.5. On the other hand, either a high flexible blade turbine or a turbine with struts at blade tips is not attractive as a rigid blade turbine in terms of energy extraction. This is an indication that very deformable blades are absolutely not efficient as used to an energy extraction device.

4. Conclusion and discussion

With a use of a fully-coupled Fluid-Structure-Interaction (FSI) method, we carried out a numerical investigation on the effect of structural flexibility of a vertical axis wind turbine blade on its passive structure deformation, unsteady external loading, internal stress analysis and the turbine energy extraction ability. For the flexible blade, two different values of effective stiffness are tested. With the real application in VAWT industry, we also studied cases with the blade support strut at two different locations.

The simulation shows that the blade bending and twist deformations vary with time periodically with one dominant frequency. Increasing tip speed ratio leads to an increase of peak values of bending and twist deformation. With the centrifugal force acting on the blade, the blade bending deflection is always pointing to the positive centrifugal force direction. The blade internal stress contours under maximum external loads are provided in the present study, which is believed to be useful for the further structure fatigue damage analysis in the industry.

Leading edge suction effect is observed in both rigid and flexible blade cases, which mainly leads to the twist motion of flexible blade, and thus enlarges the influence of LES. A large blade bending deflection with a small net pressure load onto blade surface is observed, which is induced by the opposite direction between the centrifugal force and net pressure forces applied on the flexible blade.

A larger bending and twist deflection occurs associated with a more flexible blade because of a high stress caused by the flexible deflection.

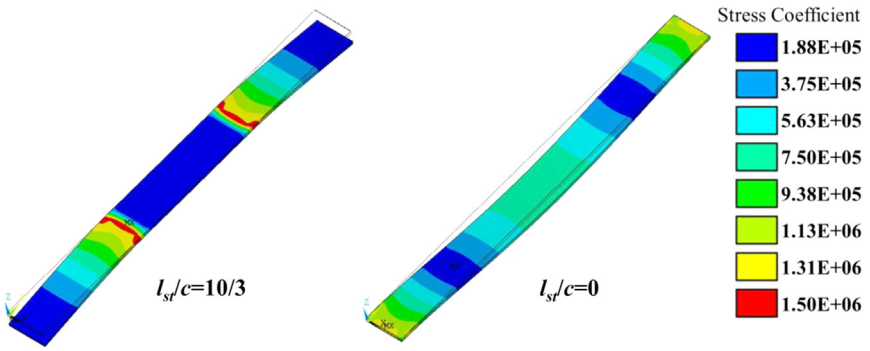

Fig. 28. Contour of stress distribution over the blade under the largest external load condition for the flexible blade with $l_{st}/c=0$, $\Pi = 3.19 \times 10^3$ and $\lambda=5.5$ viewing from the inner side of blade.

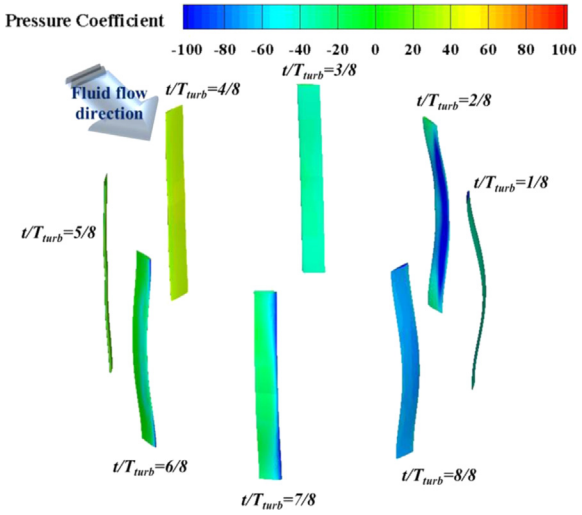

Fig. 29. Blade bend-twist motion and pressure distribution for different time instants with $l_{st}/c=0$,$\Pi = 3.19 \times 10^3$ and $\lambda=5.5$.

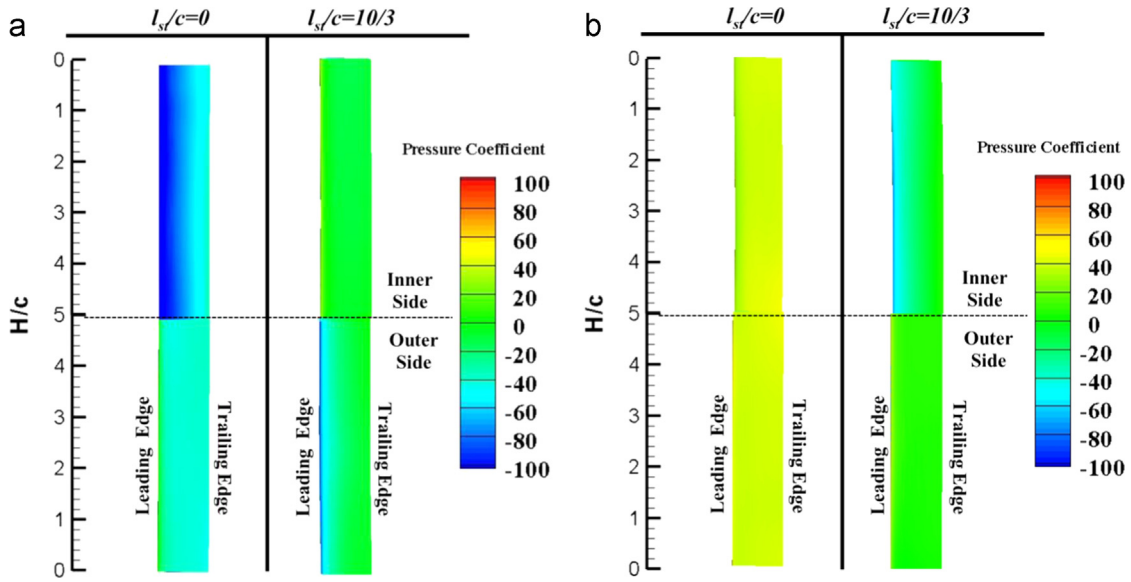

Fig. 30. Pressure distribution at (a) $t/T_{turb}=1/8$ and (b) $t/T_{turb}=4/8$ with $\lambda=5.5$, $\Pi = 3.19 \times 10^3$ and $l_{st}/c=0$ compared with $l_{st}/c=10/3$. (a) $t/T_{turb}=1/8$ (b) $t/T_{turb}=4/8$.

A blade with tip strut support shows a smaller bending deflection compared to its middle support method.

With a flexible blade, an unstable fluid field around the blade is observed which is associated with some small fluctuations in the instantaneous moment coefficient curve. At small tip speed ratio, the energy extraction efficiency is enhanced with a flexible blade. However, it becomes worse than a rigid blade counterpart at relatively large tip speed ratios.

Lastly, in our present research, we only model one blade, which is simplified from real industry where three-bladed VAWTs are very commonly used to achieve a high energy. Therefore, performing a two-bladed or three-bladed VAWT with a passively controlled bending and

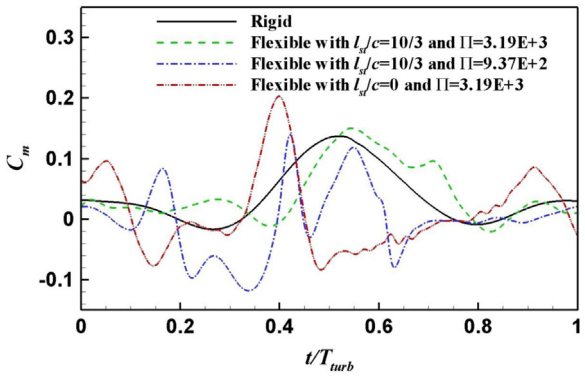

Fig. 31. Instantaneous moment coefficient at λ=5.5.

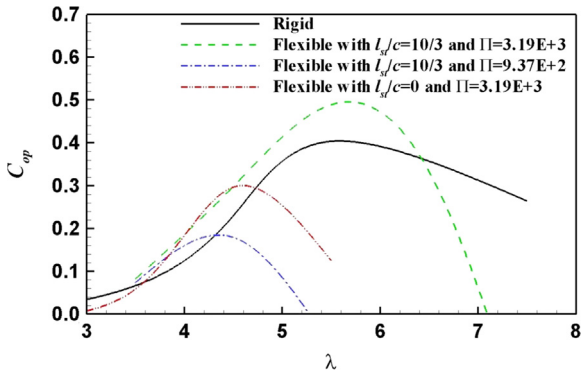

Fig. 33. Time averaged power coefficient.

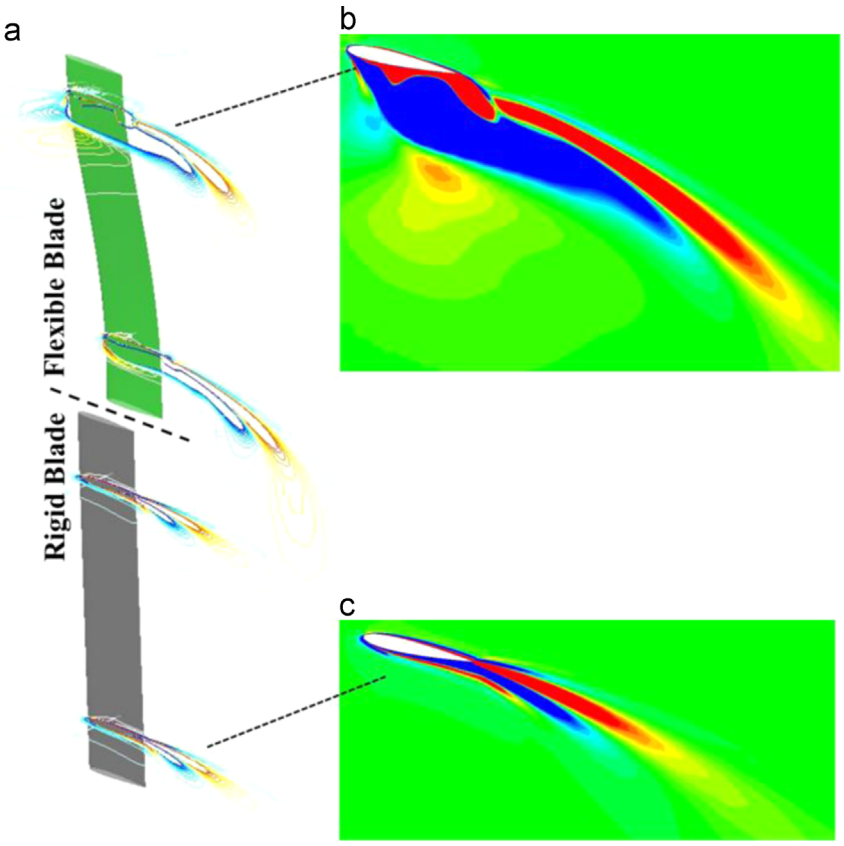

Fig. 32. Vorticity contour at t/T_{turb}=5/8 and λ=5.5.

twist is the need in our future study. Moreover, the present flexible blade deflection motion is actuated by air flow. It is believed that the blade bending/twist deflection should be different under different fluid medium (such as water). Thus, a vertical axis turbine with a passively deformed flexible blade under water condition should be investigated in the near future. A comprehensive study of the strut location impact will also be carried out in the next step.

Acknowledgments

Results were obtained using the EPSRC funded ARCHIE-WeSt High Performance Computer (www.archie-west.ac.uk). EPSRC grant no. EP/K000586/1.

References

Barlas, T., van Wingerden, J.W., Hulskamp, A., van Kuik, G., 2008. Closed-loop control wind tunnel tests on an adaptive wind turbine blade for load reduction. In: Proceedings of 46th AIAA/ASME.

Bazilevs, Y., Korobenko, A., Deng, X., Yan, J., 2015. Novel structural modeling and mesh moving techniques for advanced fluid–structure interaction simulation of wind turbines. Int. J. Numer. Methods Eng. 102 (3-4), 766–783.

Butbul, J., MacPhee, D., Beyene, A., 2015. The impact of inertial forces on morphing wind turbine blade in vertical axis configuration. Energy Convers. Manag. 91, 54–62.

Chenna, V., 2014. Fatigue-induced failure in horizontal-axis wind-turbine (HAWT) blades and HAWT drivetrain gears.

Chimakurthi, S.K., Tang, J., Palacios, R., S. Cesnik, C.E., Shyy, W., 2009. Computational aeroelasticity framework for analyzing flapping wing micro air vehicles. AIAA J. 47 (8), 1865–1878.

DeLaurier, J.D., Harris, J.M., 1982. Experimental study of oscillating-wing propulsion. J. Aircr. 19 (5), 368–373.

Gordnier, R.E., Attar, P.J., Chimakurthi, S.K., Cesnik, C.E., 2010. Implicit LES simulations of a flexible flapping wing. AIAA Paper, 2960.
Hameed, M.S., Afaq, S.K., 2013. Design and analysis of a straight bladed vertical axis wind turbine blade using analytical and numerical techniques. Ocean Eng. 57, 248–255.
Hansen, M.O., 2013. Aerodynamics of wind turbines. Routledge.
Heathcote, S., Gursul, I., 2007. Flexible flapping airfoil propulsion at low Reynolds numbers. AIAA J. 45 (5), 1066–1079.
Heathcote, S., Wang, Z., Gursul, I., 2008. Effect of spanwise flexibility on flapping wing propulsion. J. Fluids Struct. 24 (2), 183–199.
Im, H.S., Chen, X.Y., Zha, G.C., 2012. Prediction of a supersonic wing flutter boundary using a high fidelity detached eddy simulation. AIAA Paper, 39, 9–12.
Kong, C., Bang, J., Sugiyama, Y., 2005. Structural investigation of composite wind turbine blade considering various load cases and fatigue life. Energy 30 (11), 2101–2114.
Lachenal, X., Daynes, S., Weaver, P.M., 2013. Review of morphing concepts and materials for wind turbine blade applications. Wind Energy 16 (2), 283–307.
Le, T.Q., Ko, J.H., 2015. Effect of hydrofoil flexibility on the power extraction of a flapping tidal generator via two-and three-dimensional flow simulations. Renew. Energy 80, 275–285.
Liu, W., Xiao, Q., Cheng, F., 2013. A bio-inspired study on tidal energy extraction with flexible flapping wings. Bioinspir. Biomim. 8 (3), 036011.
Liu, W., Xiao, Q., Zhu, Q., 2015. A coupled fluid-structure study of the passive flexibility effect on oscillating foil energy harvester. AIAA J.
Micallef, D., Farrugia, R., Sant, T., Mollicone, P., 2014. An aerodynamic study on flexed blades for VAWT applications. In Journal of Physics: Conference Series, Vol. 555, No. 1, p. 012073, IOP Publishing.
Ponta, F.L., Jacovkis, P.M., 2001. A vortex model for Darrieus turbine using finite element techniques. Renew Energy 24 (1), 1–18.
Sadeghi, M., Liu, F., Lai, K.L., Tsai, H.M., 2004. Application of three-dimensional interfaces for data transfer in aeroelastic computations. AIAA Paper, 5376, 2004.
Scheurich, F., Brown, R.E., 2013. Modelling the aerodynamics of vertical-axis wind turbines in unsteady wind conditions. Wind Energy 16 (1), 91–107.
Shokrieh, M.M., Rafiee, R., 2006. Simulation of fatigue failure in a full composite wind turbine blade. Compos. Struct. 74 (3), 332–342.
Shyy, W., Aono, H., Chimakurthi, S.K., Trizila, P., Kang, C.K., Cesnik, C.E., Liu, H., 2010. Recent progress in flapping wing aerodynamics and aeroelasticity. Prog. Aerosp. Sci. 46 (7), 284–327.
Strickland, J.H., Webster, B.T., Nguyen, T., 1979. A vortex model of the Darrieus turbine: an analytical and experimental study. J. Fluids Eng. 101 (4), 500–505.
Strickland, J.H., Webster, B.T., Nguyen, T., 1980. Vortex model of the darrieus turbine: an analytical and experimental study. NASA STI/Recon Technical Report N. 80, 25887.
Wang, L., 2005. Theoretical and experimental study on hydrodynamic performances of vertical-axis tidal turbine (Ph.D thesis). Harbin Engineering University, China.
Wenlong, T., Baowei, S., Zhaoyong, M., 2013. Conceptual design and numerical simulations of a vertical axis water turbine used for underwater mooring platforms. International Journal of Naval Architecture and. Ocean Eng 5 (4), 625–634.
Xiao, Q., Liao, W., 2010. Numerical investigation of angle of attack profile on propulsion performance of an oscillating foil. Comput Fluids 39, 1366–1380.
Xiao, Q., Liao, W., Yang, S., Peng, Y., 2012. How motion trajectory affects energy extraction performance of a biomimic energy generator with an oscillating foil? Renew Energy 37 (1), 61–75.